Chapter 1

Voltage-Dependent Hydration and Conduction Properties of the Hydrophobic Pore of the Mechanosensitive Channel of Small Conductance

Abstract

A detailed picture of water and ion properties in small pores is important for understanding the behavior of biological ion channels. Several recent modeling studies have shown that small, hydrophobic pores exclude water and ions even if they are physically large enough to accommodate them, a mechanism called hydrophobic gating. This mechanism has been implicated in the gating of several channels, including the mechanosensitive channel of small conductance, MscS. Although the pore in the crystal structure of MscS is wide and was initially hypothesized to be open, it is lined by hydrophobic residues and may represent a nonconducting state. Molecular dynamics simulations were performed on MscS to determine whether or not the structure can conduct ions. Unlike previous simulations of hydrophobic nanopores, electric fields were applied to this system to model the transmembrane potential, which proved to be important. Although simulations without a potential resulted in a dehydrated, occluded pore, the application of a potential increased the hydration of the pore and resulted in current flow through the channel. The calculated channel conductance was in good agreement with experiment. Therefore, it is likely that the MscS crystal structure is closer to a conducting than to a nonconducting state.

INTRODUCTION

Hydrophobic Nanopores

Biological ion channels play an essential role in cell survival by providing superb control over the molecules and ions they allow to enter and leave [1]. On a very simplistic level, these channels exist in two states, an impermeable closed state and a permeable open state. A stimulus, such as ligand binding or a change in the electrical or osmotic environment of the cell, can induce a transition from a closed resting state to an open state that allows passage of a particular set of ions or molecules. An essential part of this gating process is the formation of a pore through the membrane, such that the barrier to ion passage is greatly reduced compared to that of the impermeable lipid bilayer.

The requirement for a low barrier demands the presence of water or similar coordinating groups in an ion channel pore. The selectivity filter of potassium channels, for example, is lined by backbone carbonyls that mimic the coordination of an aqueous potassium ion [2]. In contrast, less selective channels such as the nicotinic acetylcholine receptor [1], the mechanosensitive channels of large and small conductance [3, 4], and α-hemolysin [5] are thought to have open states with wider pores that support hydrated ions.

The properties of water in these small pores are very important in understanding ion channel function. The microscopic properties of water are not fully understood, and it is well established that water in narrow spaces such as might be seen in the pore of an ion channel (on the order of a few molecules across) does not necessarily have the same properties as bulk water [6]. For example, molecular dynamics (MD) studies by

Beckstein and Sansom have established the surprising result that a hydrophobic pore is

not necessarily filled with water, even if it is large enough to fit several water molecules

[7–9]. Below a threshold radius, dependent on the hydrophobicity of the pore, water is

essentially absent from a model pore even if there is space for it, producing a kind of

"hydrophobic gate." For a purely hydrophobic model pore, the threshold radius is

~4.5 Å, large enough to accommodate three water molecules [7], and the threshold for

ion occupancy of the pore is even larger (~6.5 Å) [9]. MD simulations of the

hydrophobic pores of more realistic systems showed a similar threshold behavior,

although the threshold radius varied from that in the simple model. For example, the

threshold radii for the pores of the nicotinic acetylcholine receptor and a carbon nanotube

were found to be ~4.0 and ~2.5 Å, respectively [10, 11], and were quite sensitive to the

parameterization of the interaction between the water and the pore wall, at least in the

nanotube system [12].

The Mechanosensitive Channel of Small Conductance

As part of a general program investigating bacterial ion channels, we have been

studying the bacterial mechanosensitive channel of small conductance (MscS). This

channel is gated by membrane tension, and it is thought that MscS functions as a "release

valve" for the rapid efflux of osmolytes under conditions of osmotic stress [13, 14]. In

addition, MscS is modulated by voltage and displays a slight anion preference for

conduction [4]. Despite its name, the channel shows a relatively large conductance of

~1.0 nS, consistent with the proposed function.

MscS is an interesting molecule for study for several reasons. First, as a prokaryotic mechanosensitive channel, MscS is an important model system for mechanosensation in higher organisms. In general, mechanosensitive channels have been implicated in the sensation of many different stimuli, such as touch and hearing [15]. Specifically, MscS homologues have been discovered in many kinds of organisms, even fungi and plants [16, 17], but their roles in higher organisms are only beginning to be elucidated [18]. Second, MscS is modulated by voltage [14, 19]. Voltage sensation is an important feature of many ion channels, but precise details of the mechanism remain largely unknown [20]. Last, MscS is one of only a handful of ion channels that have known crystal structures [21, 22], providing unique opportunities for structure-function studies.

The crystal structure of *E. coli* MscS has been reported by Rees and co-workers [23]. The protein is a homoheptamer of multidomain subunits of 286 amino acids in length (fig. 1.1A). From N- to C-terminus, the domain organization is as follows: a transmembrane (TM) domain comprised of three transmembrane helices, a middle-β domain that consists primarily of β-sheet, and a C-terminal α/β-domain (fig. 1.1B). There are vestibules on either side of the pore: the periplasmic vestibule, lined by the N-terminal halves of TM3, and the cytoplasmic vestibule, surrounded by the middle-β and C-terminal domains. The narrowest constriction, which shall hereafter be called the pore, is the region around two hydrophobic residues, L105 and L109 of TM3, near the cytoplasmic side of the bilayer. At its narrowest point, MscS displays a pore radius of ~3.5 Å. Because the pore is physically wide enough for the passage of water and ions, it was initially hypothesized that the crystal structure is a model of the open state of the
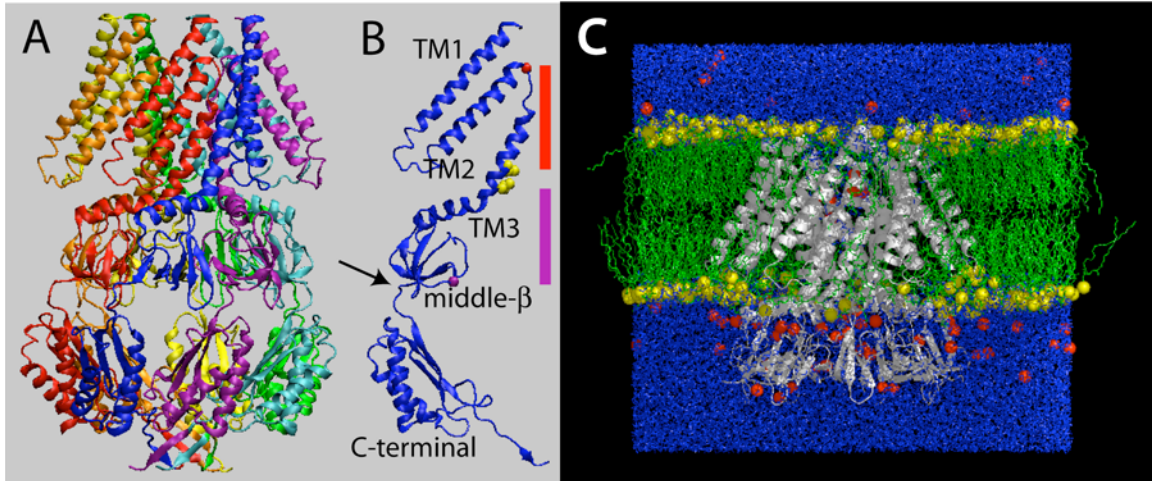
Fig. 1.1. *A*, Side view of the MscS homoheptamer, colored by subunit. *B*, An individual subunit with domains labeled. Yellow: sidechains of pore-lining L105 and L109; Red sphere: Cα of V91, the upper boundary of the periplasmic vestibule; Purple sphere: Cα of G140, the lower boundary of the cytoplasmic vestibule in the truncated MscS model. The red and purple boxes mark the approximate regions of the periplasmic and cytoplasmic vestibules, respectively. The arrow marks the end of the middle-β domain, the terminus of the simulated protein. *C*, The periodic box of the MD simulation system, showing the protein (white), phospholipid chains (green), phospholipid headgroups (yellow), water molecules (blue), and ions (red).

channel [23]. However, as noted above, 3.5 Å is slightly lower than the threshold radius for a hydrophobic gate determined by Beckstein and Sansom [7], suggesting that the structure is nonconducting.

Because of the usefulness of MscS as a model for mechanosensation and voltage modulation, an important question is whether the image of MscS produced by crystallography represents an open, conducting state of the channel or a nonconducting state. As we had done with the mechanosensitive channel of large conductance [24, 25], we turned to full-scale MD simulations of MscS to illuminate this problem. The simulation system, consisting of MscS surrounded by explicit lipid, water, and ions, is shown in fig. 1.1C.

Previous Simulations of MscS

While our efforts were in progress, two other MD simulations of MscS appeared. The first of these, reported by Anishkin and Sukharev, involved a somewhat simplified model that included only the channel-lining regions of the protein, harmonically restrained, and an octane slab to model the lipid [26]. They found that the pore was generally empty of water, and even when the pore was occupied, there was rarely more than a single file of water molecules. Furthermore, when a chloride ion was forced through the mostly dehydrated pore, it experienced a large barrier to conduction. Anishkin and Sukharev concluded that, because the relatively large conductance of MscS demands a much lower barrier than that observed in their simulations, the crystal structure is a nonconducting state with a hydrophobic gate.

Sotomayor and Schulten reported much larger-scale simulations of MscS involving full-length protein with an explicit lipid bilayer [27]. Like Anishkin and Sukharev, they found that simulations with a substantially restrained protein backbone produced a dehydrated pore region. Relaxing the restraints caused the protein to collapse, producing an occluded pore that is certainly nonconducting. However, when a large tension was applied to the system, the collapse was avoided, and a system with a substantially hydrated pore emerged.

Here we present the results of our MD simulations of MscS that were intended to shed light on whether or not the crystal structure is conducting or nonconducting, as well as provide further insights on the nature of hydrophobic pores. Our approach more nearly parallels that of Sotomayor and Schulten [27], in that we simulate nearly the entire protein in an explicit bilayer (fig. 1.1C). An informative addition in the present

simulations is an evaluation of the effect of an applied voltage on the MscS system. We

find that an applied voltage can profoundly influence the hydration of the channel,

whether in a restrained or unrestrained simulation. In addition, we find that an applied

voltage can favor a hydrated state of the channel that, even during these relatively short

simulation times, conducts a significant number of chloride ions. These results suggest

that the image of MscS obtained from crystallography is likely more similar to an open,

conducting state than to a nonconducting state.


RESULTS AND DISCUSSION

A large number of MD simulations of MscS were performed in a variety of

conditions. Fig. 1.2 summarizes the simulations, indicating for each the salt content,

presence or absence of restraints, initial pore state, and start and end times. The

stabilization of the RMS deviations (RMSDs) of the protein from the crystal structure and

the total system energies indicates that the simulations rapidly ($<$ 2 ns) attained a steady

state, as expected (fig. 1.3).

Water Occupancy of the Pore in Unperturbed MscS

The initial simulations (R^h0; R indicating a restrained protein backbone; h

indicating an initially hydrated pore; 0 indicating zero applied voltage) included soft

harmonic position restraints on all protein backbone atoms, using the same restraining

force constant [418.4 kJ/(mol nm^2)] as in previous studies [26, 27]. Even though the pore

of the restrained system was initially hydrated, it emptied of water rapidly (in ~0.5 ns).

The pore occasionally filled with water for periods of 200 or 300 ps, but for most of the
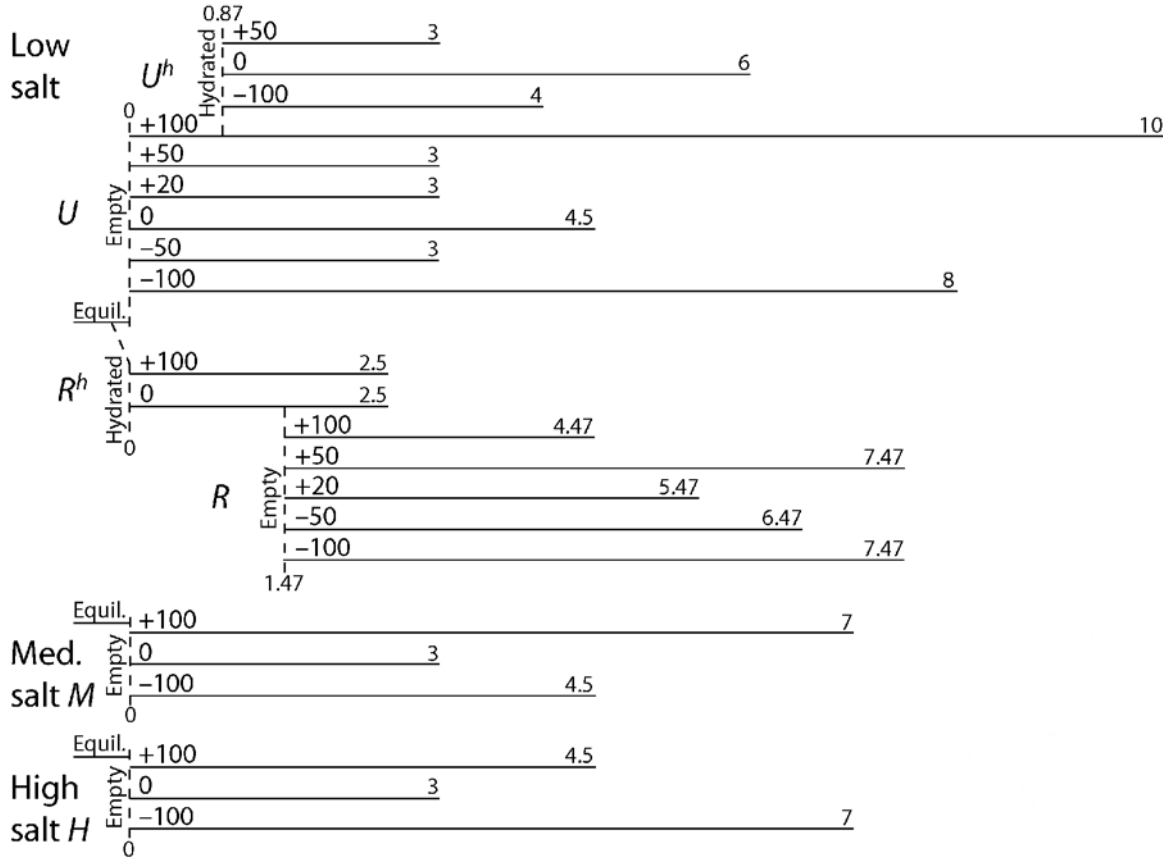
Fig. 1.2. Schematic of all wild-type simulations, indicating their salt content, initial hydration state (R^h, U^h: hydrated; R, U, M, H: empty), presence of restraints (R: restrained; U, M, H: unrestrained), applied electric field (in mV/nm), and start and end times (in ns).
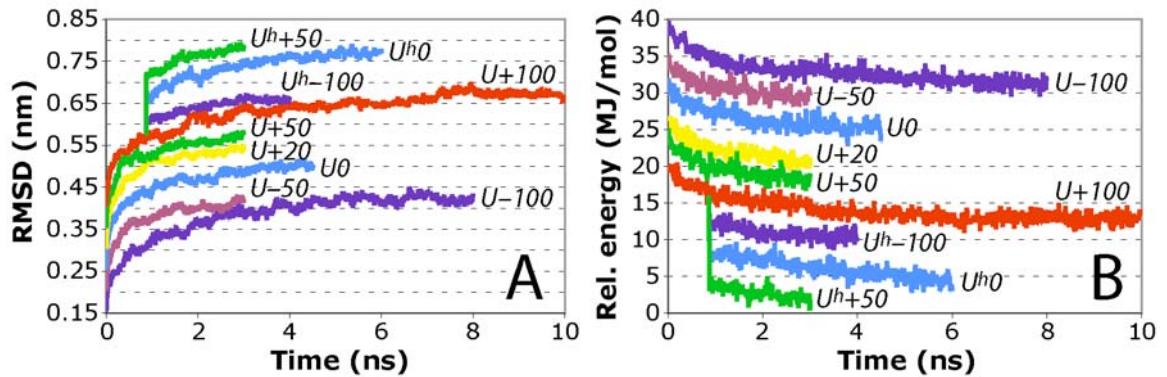
Fig. 1.3. Equilibration of wild-type simulations. RMS deviations (RMSDs) (*A*) and total energies (*B*) are shown as a function of time. For clarity, the RMSDs of the different simulations are offset in steps of 0.05 nm, and the energies are offset in steps of 4 MJ/mol. Most simulations have reached a steady state by ~2 ns.
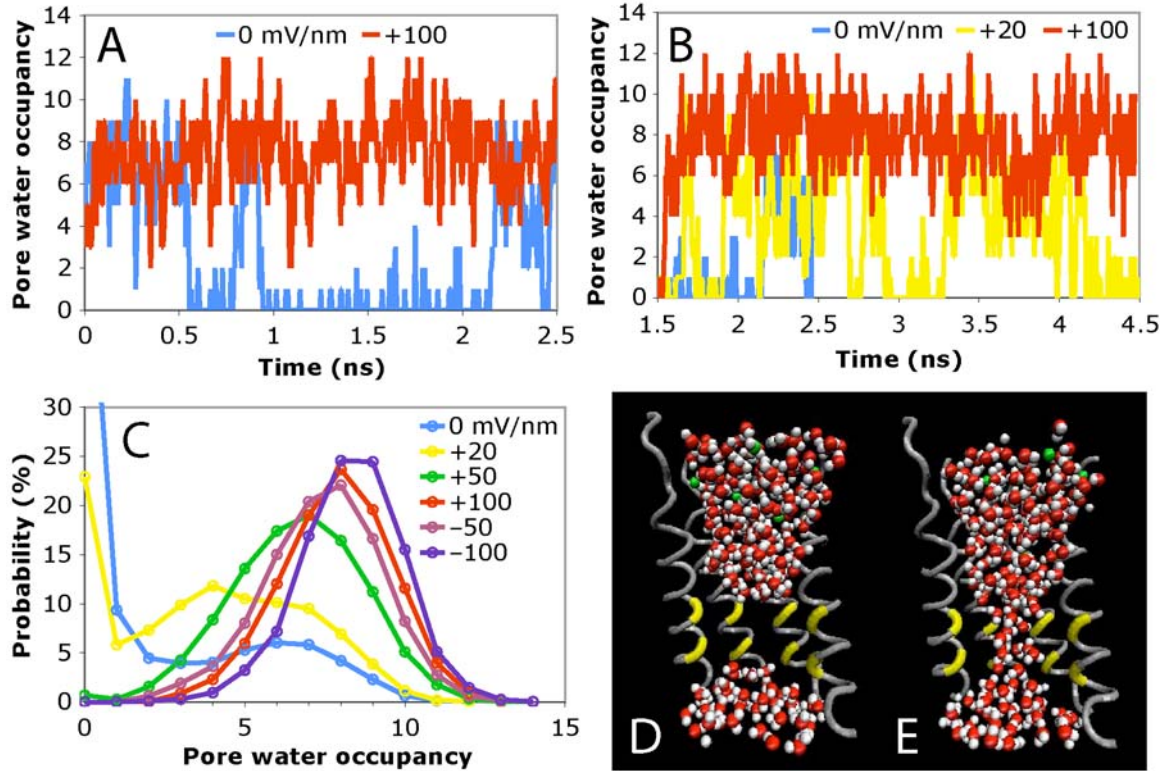
Fig. 1.4. *A–B*, The water occupancy of the pore as a function of time in R^h (*A*) and *R* (*B*) simulations with various electric fields. For clarity, *R+50*, *R–50*, and *R–100* are not included in *B*. They have water behavior very similar to *R+100* (red). *C*, Probability distributions of water occupancy in *R* and R^h for various electric fields. *D–E*, Snapshots of the pore viewed from the side in a dehydrated (*D*) and fully hydrated (*E*) state. The gray helices are the N-terminal halves of the TM3 helices, which line the channel. For clarity, only four of the seven helices are shown. The locations of the pore-lining leucines are shown in yellow. Water molecules (red and white) and chloride ions (green) are shown as spheres.

simulation, it was completely empty (fig. 1.4A, blue trace). The water was separated by the hydrophobic region into two distinct reservoirs (fig. 1.4D). These results are consistent with previous simulations of hydrophobic nanopores, because the size of the MscS pore is smaller than the threshold for hydration [7, 8].

Removing the restraining force did not change the hydration behavior of the system. Whether the initial state was empty (*U0*; *U* indicating an unrestrained protein backbone) or hydrated (*U^h0*), the pore quickly evolved into a dehydrated state
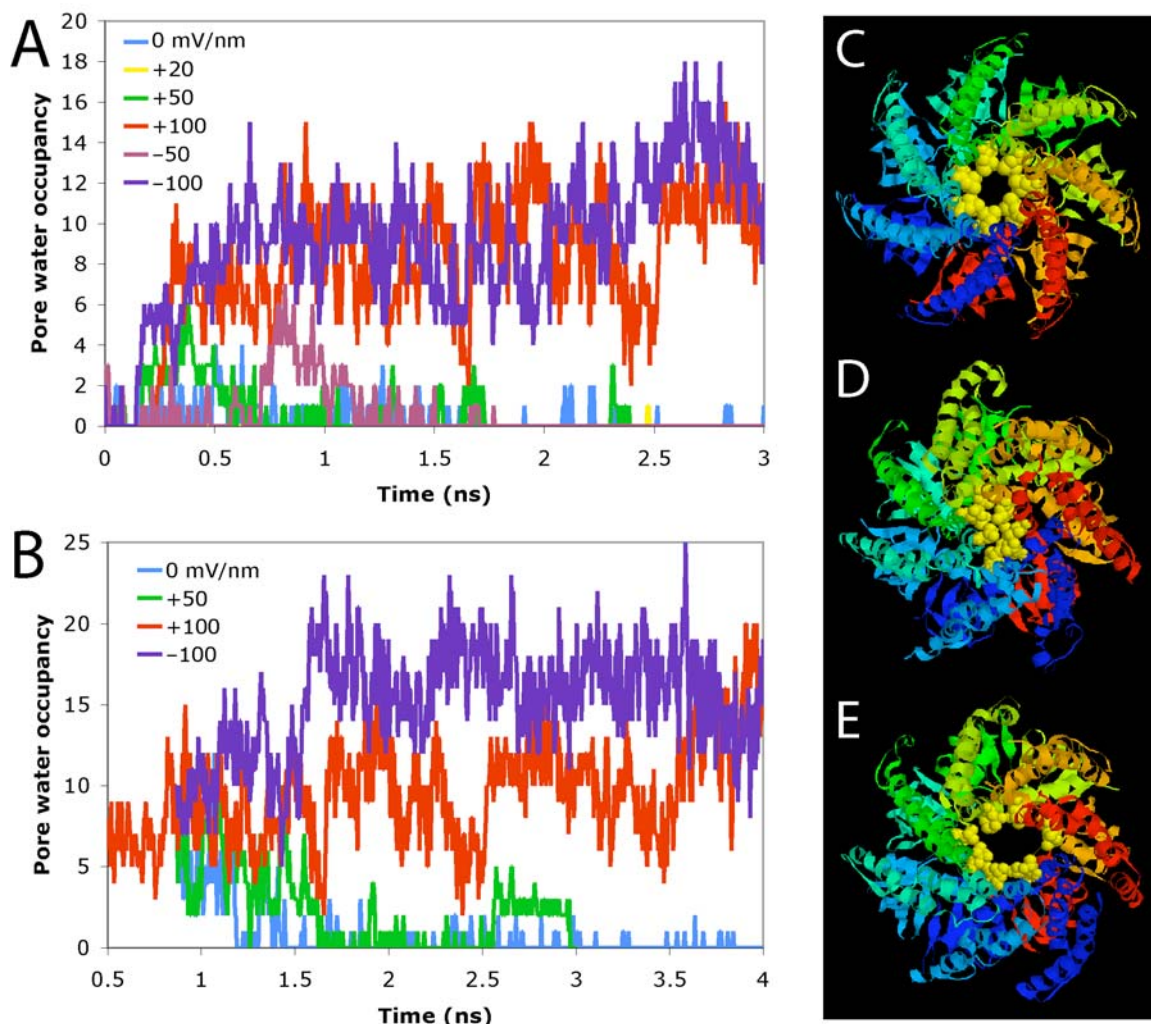
Fig. 1.5. *A–B*, The water occupancy of the pore as a function of time in *U* (*A*) and *U^h* (*B*) simulations with different electric fields. *C–E*, Snapshots of the pore viewed from the periplasm. *C* shows the crystal structure, and *D* and *E* show frames from the end of *U0* and *U+100*, respectively. The protein is colored by subunit, except L105 and L109, which are in yellow spacefilling.

(fig. 1.5A–B, blue traces). Because the dehydration effectively produced a local vacuum

(fig. 1.4D) and there were no restraints on the protein, the pore rapidly collapsed. In clear

contrast to the crystal structure, which contains a wide pore (fig. 1.5C), this collapsed

structure displayed an essentially complete occlusion of the channel, formed by L105 and

L109 of TM3 (fig. 1.5D). It is certain that such a structure represents a closed,

nonconducting form of the channel. These results completely parallel those of

Sotomayor and Schulten, who also considered an explicit bilayer and a fairly complete model of the protein [27]. Given that the present work employs a different force field and simulation package from that of Sotomayor and Schulten, the similarities are gratifying and enhance the confidence in the overall behavior of the system.

Application of a Voltage to the Simulation System

As noted above, along with being responsive to changes in membrane tension, the behavior of MscS is significantly perturbed by alterations in transmembrane voltage [14]. Given the intense interest in the molecular mechanism of voltage sensing in ion channels in general and Kv channels in particular [20, 22, 28–31], we found this to be one of the most attractive features of the MscS channel. We, and others, were especially intrigued by the presence of a number of arginine residues in the transmembrane domain of MscS [23]. Arginine residues play a critical role in voltage sensing in the Kv channels, and we have sought, both experimentally and computationally, to probe their role in MscS. Of course, in its natural environment MscS is always exposed to a significant transmembrane voltage. In fact, bacterial transmembrane potentials are unusually high, perhaps in the range of –120 to –160 mV, or more [32]. Also, all experimental studies of MscS using the patch-clamp methodology require a transmembrane potential to see conduction.

We began by subjecting the system with harmonic restraints to an applied electric field of +100 mV/nm. The sign convention is such that a negative electric field produces a bias that is in the same direction as a natural transmembrane potential; the inside of the cell is negative relative to the outside. Therefore, with this field, our simulation

represents a depolarized membrane. Under these conditions with an initially hydrated

pore (R^h+*100*), the pore remained hydrated for the entirety of the simulation (fig. 1.4A,

red trace). There was a continuous column of water molecules throughout the pore

region (fig. 1.4E). In addition, the initially empty pore of *R+100* became hydrated very

rapidly (~0.1 ns) (fig. 1.4B, red trace). Again, the observation of the same steady-state

behavior with different initial conditions indicates the robustness of the result. Thus, the

application of a voltage to the system has qualitatively altered the behavior of the

channel.

The +100 mV/nm field is relatively large. We therefore considered smaller

potentials and the consequence of reversing the field. As we saw in *R+100*, the presence

of other moderate or high electric fields (±50 or –100 mV/nm) allowed rapid filling to

create a hydrated pore, and the pore remained hydrated for essentially the entire length of

the simulations. For a more modest field of +20 mV/nm, the pore displayed more

frequent dewetting events, but we still observed increased hydration compared to

simulations with no field (fig. 1.4B). Thus, an extraordinarily high field is not required to

see qualitatively different wetting behaviors from the restrained simulations of Anishkin

and Sukharev [26] or Sotomayor and Schulten [27]. The hydrophobic gate of MscS seen

in previous simulations is absent in the presence of a potential.

The probability distribution for water in the pore for each of the six electric fields

clearly indicates a field dependence on the amount of water hydrating the pore in the

restrained simulations (fig. 1.4C). Without a field, there is very little water in the pore,

but as the magnitude of the field increases the pore is more likely to be hydrated. Electric

field effects on the threshold radii for model hydrophobic gates have not yet been studied,

but the data here strongly suggest that increasing the electric field reduces the threshold radius.

We next considered the effects of an applied voltage on the unrestrained system. Simulations with electric fields of ±100 mV/nm (*U±100*) displayed qualitatively similar water behavior to *R±100*, with one important difference. When beginning from a dehydrated pore, the unrestrained simulations revealed a competition between water and the pore-lining leucines to fill the vacuum in the pore. The inherently chaotic behavior of MD was especially evident here, in that subtle differences in the simulations led to two distinct pore states. The *U+100* and *U–100* simulations were each performed several times, on different computer environments (fig. 1.6A–D). In some simulations, inward collapse of the leucines resulted in an occluded pore (like that seen in *U0*, fig. 1.5D) that contained no water. However, in other simulations, water entered the pore first and formed a stably hydrated state. Clearly, the pore state is very sensitive to the initial conditions of the simulations. Similar chaotic behavior involving the competition between the water and the leucines was seen in other simulations, discussed below. However, it is notable that once a certain threshold of hydration was attained by the pore (~5 water molecules), the channel remained fully hydrated throughout the simulation (fig. 1.6A–D; the red and purple traces in fig. 1.5A–B are representative examples of the simulations that contained stably hydrated pores).

In the simulations with a stably hydrated pore (*U+100*, *U–100*, *U^h–100*), the water prevented the collapse of the pore-lining leucines and maintained a pore approximately the same size as that of the crystal structure (fig. 1.5E). Because there were no restraints on the protein conformation, the pore was free to widen slightly and
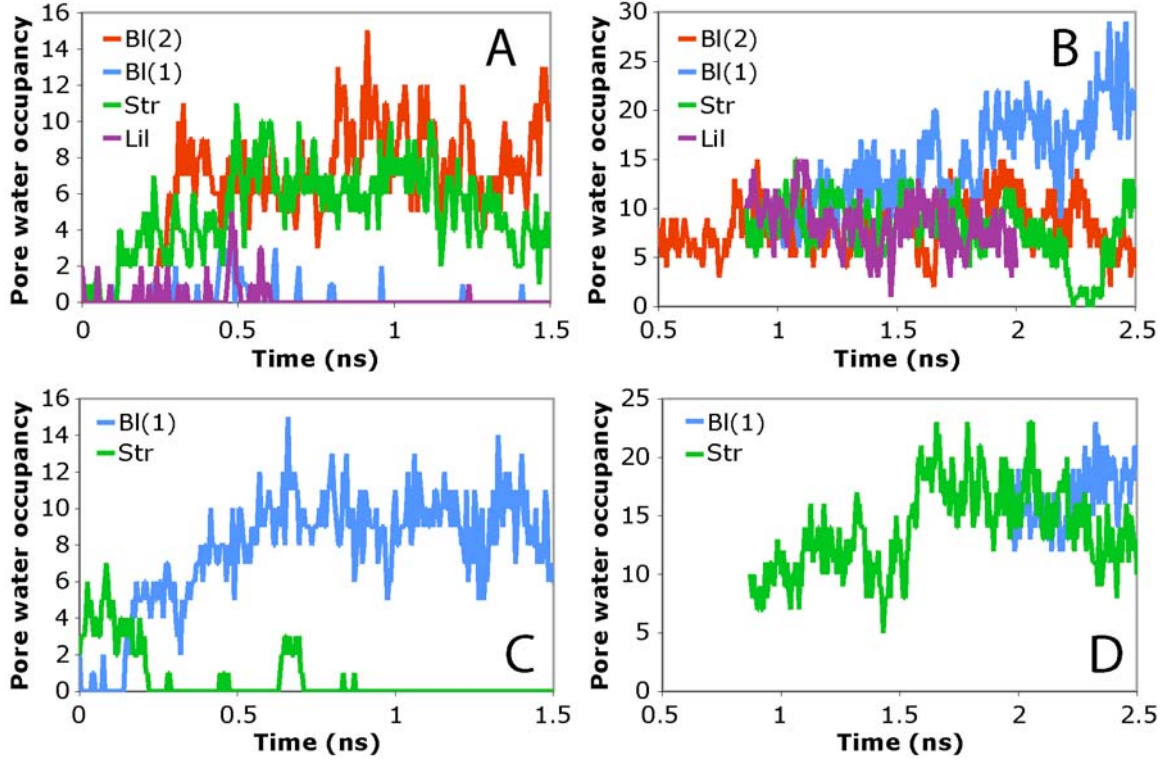
Fig. 1.6. Pore hydration of simulations from different computer environments. The data in each graph are from simulations with identical input parameters; only the computer environments differed. All simulations are unrestrained with an electric field of +100 (*A–B*) or –100 mV/nm (*C–D*). The pore was initially empty in *A* and *C* and hydrated in *B* and *D*. The computer environments used were as follows: Bl(2): Blackrider using two processors; Bl(1): Blackrider using one processor; Str: Strongbad using one processor; Lil: Liligor using one processor. Bl(2) in *A* was selected as the representative simulation *U+100*, Bl(1) in *C* as *U–100*, and Bl(1) in *D* as $U^h–100$.

accommodate more water molecules than were present in the restrained simulations. As in the restrained simulations, a large potential stabilized a hydrated pore, further suggesting that MscS does not have a hydrophobic gate in a high electric field. Again, the results here are analogous to the work of Sotomayor and Schulten, who demonstrated that membrane tension, like the transmembrane potential in our simulation, is sufficient to maintain a wide, hydrated MscS pore [27]. It should be mentioned that voltage and tension affect MscS in different ways. Tension is the primary stimulus for activation, but

recent electrophysiological results indicated that voltage modulates its deactivation [19]. However, it is interesting that both tension and voltage are separately sufficient to maintain the pore state of the crystal structure.

However, a notable difference between the restrained and unrestrained simulations was observed with applied fields of lower magnitudes (+50 to –50 mV/nm). Field-dependent hydration of the pore was not observed in these unrestrained simulations. Instead, with lower fields, the system quickly evolved into the dehydrated, collapsed state, regardless of whether the pore was initially empty or hydrated (fig. 1.5A–B).

The fact that the hydration state of the pore is dependent on its flexibility, as observed in our simulations with +20 or ±50 mV/nm fields, is in agreement with recent work by Beckstein and Sansom that showed a general inverse relationship between the flexibility of a hydrophobic pore and the probability of water occupancy [9]. They attributed this phenomenon to a decrease in the depth of the attractive well of the van der Waals potential of a water molecule interacting with the fluctuating walls. The results here suggest that in moderate electric fields, the shallower wells destabilize the water to the point that the field energy is no longer sufficient to maintain a hydrated pore. However, large fields of ±100 mV/nm maintain a hydrated MscS pore even with no restraints at all.

We hypothesized that the mechanism by which a large field contributes to pore hydration involves the field-induced alignment of water dipoles in the pore. Snapshots of water in the pore clearly showed a field-dependent alignment (fig. 1.7A–C). We quantified this by plotting the alignment of the water ($\langle \cos \theta \rangle$, where θ is the angle between the water dipole and the z-axis) as a function of position in the periodic box for
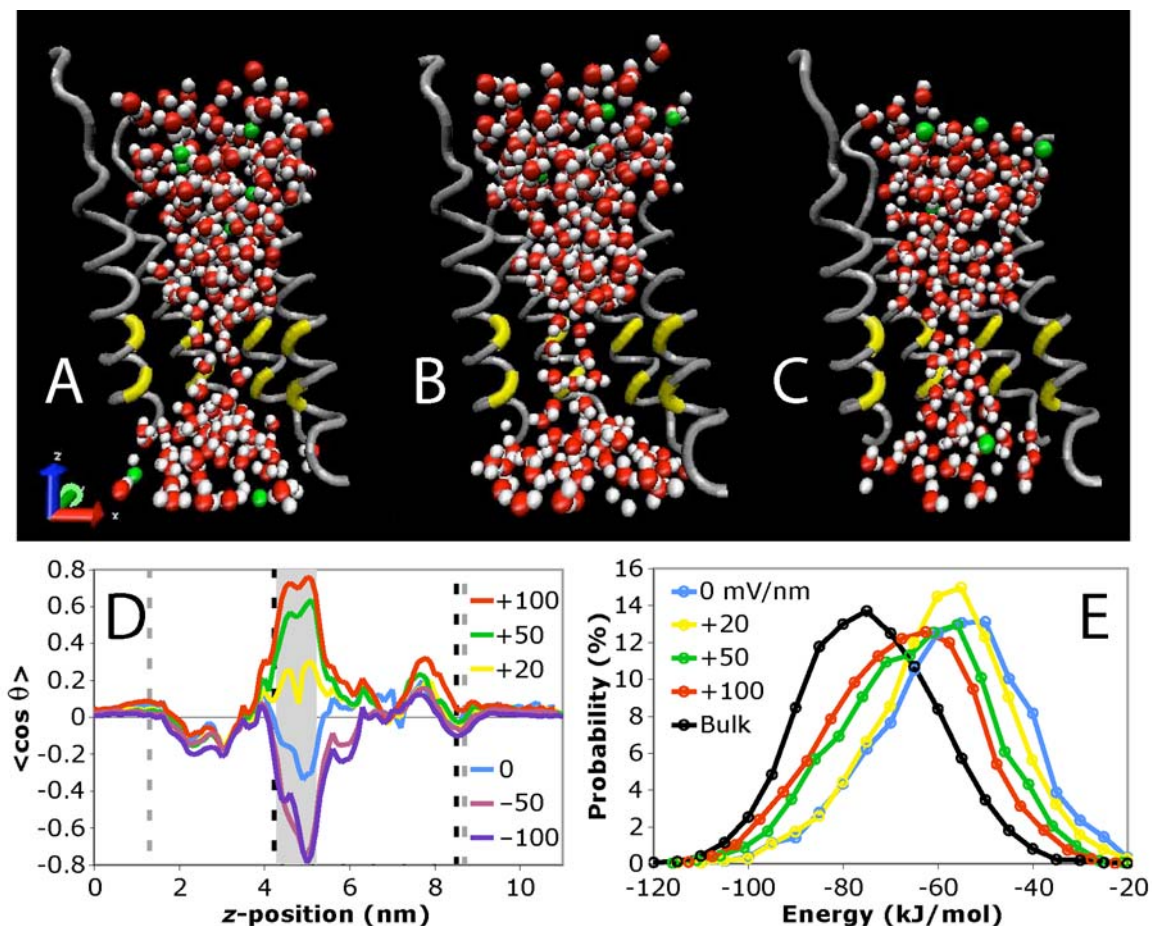
Fig. 1.7. *A–C*, Snapshots of the pore viewed from the side in *R+100* (*A*), *R0* (*B*), and *R–100* (*C*), indicating the high degree of water alignment. The coloring is described in fig. 1.3D–E. The system axes are shown on the left. *D*, Net alignment of water dipoles as a function of position within the simulation system for various electric fields. To minimize the influence of water molecules that have a *z* value corresponding to the pore region but that are in fact embedded in the membrane, only water molecules that occupied the pore at some point in the simulation are considered. Important regions are marked as follows: Light gray vertical stripe: pore region; black dashed vertical stripes: the limits of the bilayer; gray dashed vertical stripes: the limits of the protein. *E*, Probability distributions of interaction energies of water molecules in the bulk and pore regions under the application of various electric fields. Dipole-field interactions are included in the energies. All data are from *R* and R^h simulations.

the *R* simulations (fig. 1.7D). In the regions near the edge of the box, in which the

environment is most similar to bulk water, the water shows only a slight orientational

preference, which is independent of the applied field. The fact that there is no field-

dependence to the alignment is not surprising, because the dipole orientation energy of an

individual water molecule in even the largest electric field is only one-sixth of kT. The small nonzero net dipole in these regions is likely an artifact of the periodic boundary conditions, as recently reported [33]. The large dipoles of MscS and its infinite images lead to ordering of the water structure even in the bulk regions. In other regions of the simulation system, local interactions between polar groups in the protein and bilayer tend to orient the water in a field-independent manner.

The pore region, however, is unique in that there is a large field dependence on the alignment of the water. The alignment of the water correlates reasonably well with the water occupancy of the pore, with the 0 and +20 mV/nm fields showing a relatively poor alignment compared to the ±50 and ±100 mV/nm fields. In the ±100 mV/nm fields, the absolute values of $\langle \cos \theta \rangle$ approach 0.8, a very high degree of alignment.

The observation of water alignment in stronger fields provides an explanation for the influence of an external field on pore hydration. In a hydrophobic pore, a water molecule oriented with its dipole parallel to the pore interacts through hydrogen bonds with the water molecules above and below it. Rotation of this dipole toward the wall of the pore is unfavorable, because the weak interaction between the water and the hydrophobic wall does not compensate for the energy lost from the weakened hydrogen bonds with the waters above and below.

The enthalpic gain from hydrogen bonding in forming a water column in a hydrophobic pore comes with an entropic penalty for forming such an ordered structure. In the present system, the enthalpy of the hydrogen bonding alone is insufficient to overcome this cost, as evidenced by the fact that in the absence of an electric field, a hydrated pore occurs only rarely. However, an electric field provides further stability for

the water column, in that the orientation energy of the several aligned water dipoles contributes favorably to the enthalpy, and the overall energy is lowered in a field-dependent manner. This can clearly be seen by comparing the interaction energy distributions for water in the pore in the various electric fields (fig. 1.7E). The energy distributions from the different fields form approximately Gaussian curves, all with about the same width. However, with an increasing field (and increasing alignment), the midpoints of these distributions are shifted toward lower energies, and the interaction energies approach those for bulk water. For an individual molecule, the dipole orientation energy is small, as mentioned earlier, but for several molecules, the energy becomes more significant. In this way, a hydrated pore is preferentially stabilized by larger electric fields.

The degree of alignment of the water with no applied electric field gives a sense of the strength of the electric field inherent to the protein itself. The pore is lined by seven α-helices, all with their helical dipoles pointing generally in the $+z$ direction. Dipole-dipole interactions favor an arrangement of water oriented with its dipole in the $-z$ direction, exactly as observed in our simulations. This may be why, in the R simulations, the -50 and -100 mV/nm fields had slightly greater hydration than the $+50$ and $+100$ mV/nm fields, respectively (fig. 1.4C).

Pore Water Occupancy with Higher Salt Concentrations

Unrestrained simulations with higher salt concentrations (200 and 300 mM instead of 100 mM; designated as M and H, for medium and high salt) and fields of $+100$, 0, and -100 mV/nm were also performed and compared to the low-salt (U) simulations.
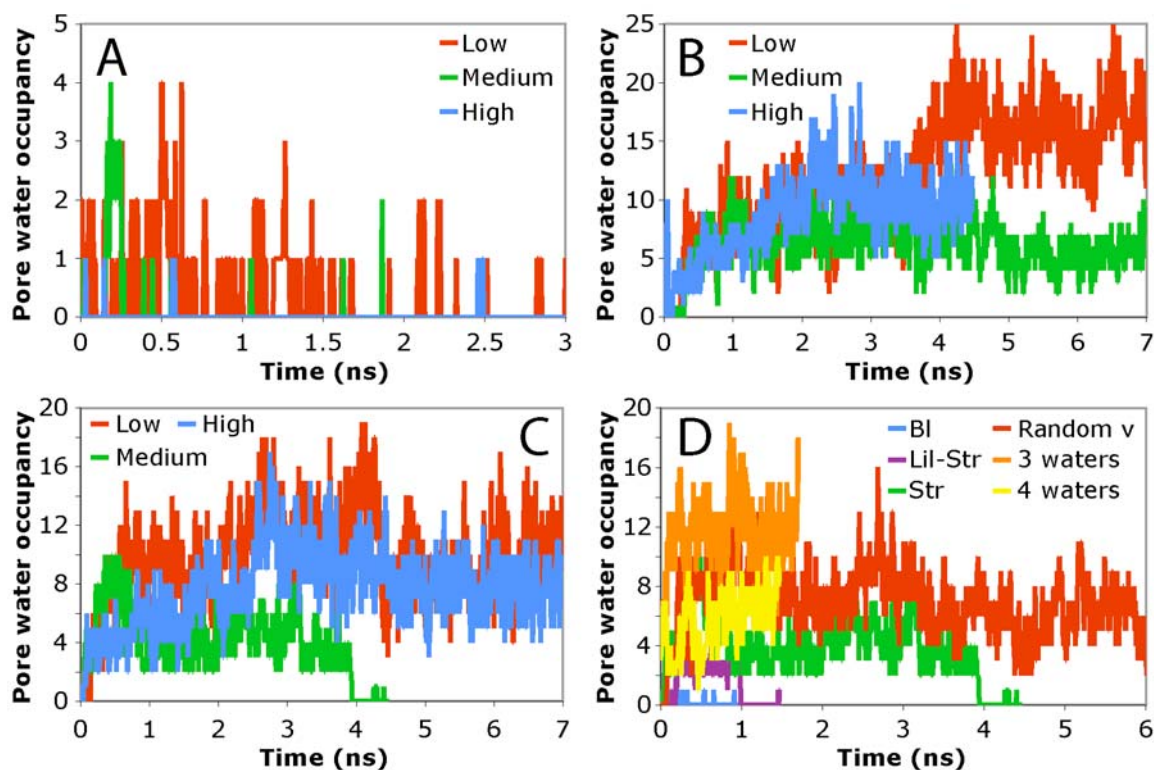
Fig. 1.8. *A–C*, The water occupancy of the pore as a function of time for simulations with fields of 0 (*A*), +100 (*B*), and –100 mV/nm (*C*). *D*, Pore water occupancy for *M–100* simulations in different conditions. The first three represent "continuation simulations" with identical input parameters on different computer systems (Bl: Blackrider; Lil-Str: started on Liligor, but later transferred to Strongbad; Str: Strongbad). The last three represent "altered simulations" with slightly altered initial arrangements. In Random v, the velocities of all the atoms were randomized at the beginning of the simulation. In 3 waters and 4 waters, three or four water molecules were manually inserted into the pore at the beginning of the simulation.

For the most part, the salt concentration did not significantly affect the water occupancy of the pore. In *M0* and *H0*, the pore remained in a dehydrated state and quickly became occluded by the pore-lining leucines, just as it did in *U0* (fig. 1.8A). Also, in *H±100*, as in *U±100*, the pore remained hydrated for essentially the full length of the simulations (fig. 1.8B–C). However, the results of the *M±100* were slightly different from expected. Although the pore remained stably hydrated throughout *M+100*, there was generally less water in the pore than in *U+100* or *H+100* (fig. 1.8B–C). Even more unusual, the pore in *M–100* emptied of water and became occluded after it had been substantially hydrated,

which contrasted with *U±100*, *H±100*, and *M+100*. In these simulations, when the pores

attained a threshold level of hydration (~5 waters), they remained fully hydrated

throughout the simulation.

Therefore, the *M–100* results were explored more fully by observing the pore

water occupancy in simulations with slightly different conditions. Three "continuation

simulations," which began with identical atom positions and velocities, were performed

on different computer systems. Also, three "altered simulations" were performed. For

two of these, three or four waters were added to the pore at the beginning of the

simulations. For the third, the atom velocities at the beginning of the simulation were

randomized. The velocities still reflected a system temperature of 310 K, like the other

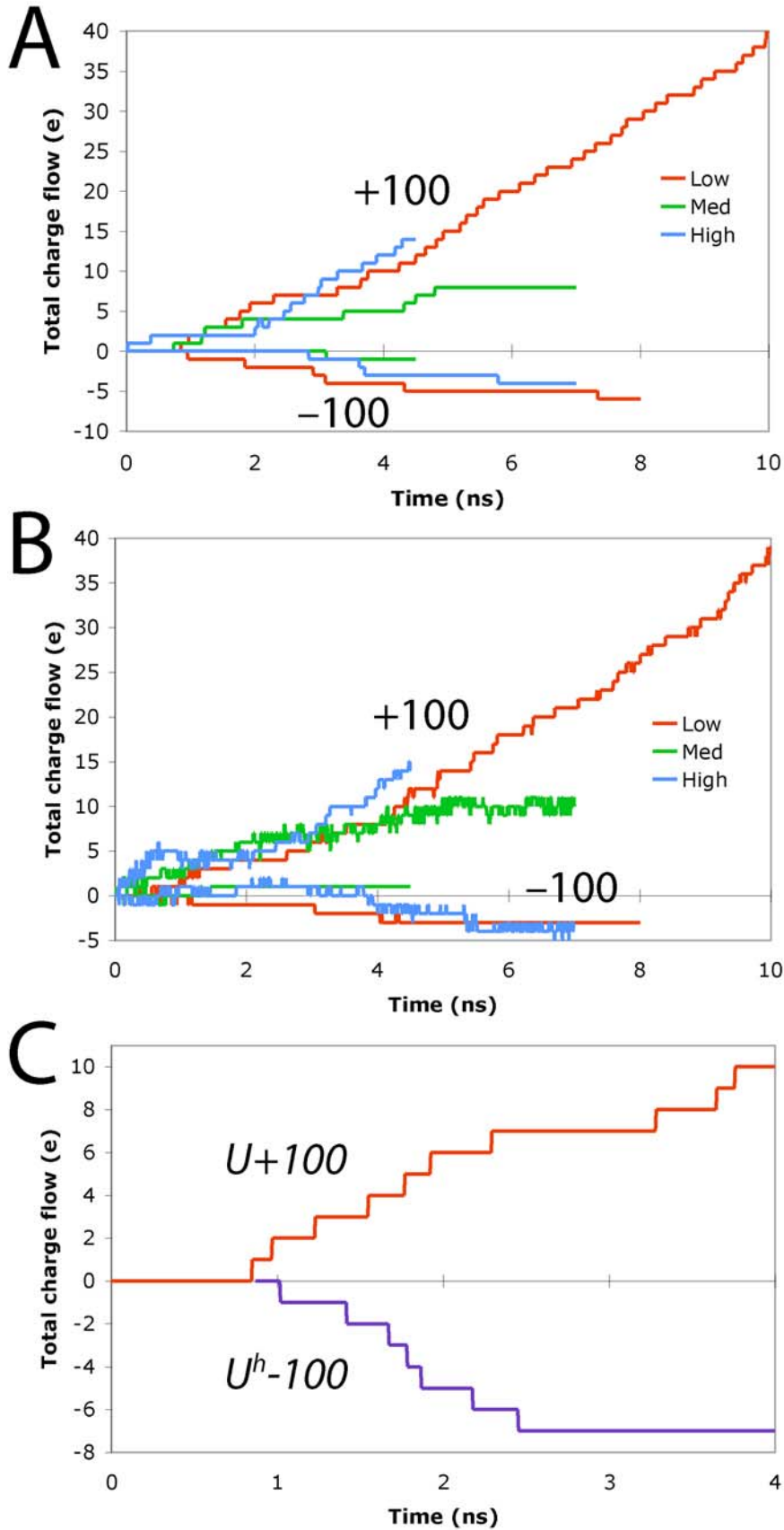simulations, but different velocities were assigned to each atom.

As seen in *U±100*, the continuation simulations displayed chaotic behavior

involving the competition between the water and the pore-lining leucines to fill the

evacuated pore (fig. 1.8D). In two continuation simulations, a hydrated pore was never

attained before occlusion occurred. In the third continuation simulation, a hydrated pore

emerged but eventually dehydrated, which, as mentioned earlier, was unexpected.

However, the water in the altered simulations, in which the initial state of the system was

slightly different, behaved like it had in previous simulations. In all three, the pore filled

with water and remained hydrated for the full length of the simulations (fig. 1.8D). The

emptying of the hydrated pore in *M–100* was not consistently observed, suggesting that

the one case where it occurred was anomalous. Therefore, the simulations with medium

and high salt strengthened the idea suggested by the low-salt simulations that a field of

±100 mV/nm is sufficient to stably hydrate the MscS pore.

A possible explanation for the unexpected results from the *M* simulations is that concentrated salt solutions have an increased surface tension, thereby preferentially stabilizing the liquid-vacuum interface of the dehydrated pore. This explanation was invoked by Anishkin and Sukharev for their observation that the pore water occupancy in their simulations was somewhat lower in 150 mM NaCl solution than in pure water [26]. This is consistent with the relationship between the *M* and *U* simulations, but not of that between the *H* and *M* or *H* and *U* simulations. Therefore, the discrepancies in the pore hydration of the *U*, *M*, and *H* simulations are still not completely understood.

Spontaneous Conduction of Ions Through the Hydrated Channel

A stably hydrated pore is necessary but not sufficient for ion conduction through the MscS crystal structure. Sotomayor and Schulten's work showed that membrane tension could oppose collapse and produce a hydrated channel, but no ionic conduction was seen in their simulations [27]. However, in the present simulations, the application of a transmembrane potential provides a natural driving force for ions to pass through the channel. Indeed, we observe a significant number of spontaneous ion transits through the channel when a voltage is applied.

We define a conduction event as the movement of an ion through the full length of the pore. For each simulation, a running total of the number of conduction events can be plotted as a function of time; on such a plot, a constant current is characterized by a more or less linear function. An approximation of the current can be calculated by dividing the number of events by the time between the first and last event. The most compelling case is *U+100*. Fig. 1.9A (upper red trace) shows that many conduction

Fig. 1.9. *A–B*, Total charge flow by conduction (*A*) and diffusion (*B*) as a function of time for unrestrained simulations in low, medium, and high salt. Fields of both +100 (positive charge movements) and –100 mV/nm (negative charge movements) are represented. Steady-state times (in ns) are as follows: *A*, *U+100*: 3.285–9.965; *M+100*: 3.380–4.805; *H+100*: 2.005–4.295; *U–100*: 4–8; *M–100*: 2–4.5; *H–100*: 2.840–5.790; *B*, *U+100*: 4.140–9.955; *M+100*: 2.780–4.995; *H+100*: 2.450–4.480; *U–100*: 4.04–8; *M–100*: 0–4.5; *H–100*: 2.945–6.700. *C*, Comparison of total conductive charge flow in *U+100* and U^h–100.

Table 1.1. Conduction and diffusion current data calculated from all wild-type MscS simulations that contained at least one conduction event

Simulation(s)	Field mV/nm	ΔV_z mV	Total Time ns	Conduction Current			Diffusion Current	
				Total Events[a]	Steady State[b]		Total Events[a]	St. State[b]
					I pA	g nS		I pA
R+50	+50	+550	6.0	1	Low[c]	Low	1	Low
R+100, R^h+100	+100	+1100	5.5	11	410	0.37	9	450
U+100			10.0	40	790	0.72	39	850
M+100			7.0	8	450	0.41	11	290
H+100			4.5	14	840	0.76	15	790
R–100	–100	–1100	6.0	2	Low	Low	1	0
U–100, U^h–100			11.1	13	Low	Low	5	0
M–100			4.5	1	Low	Low	1	0
H–100			7.0	4	–220	0.20	7	–260

[a] All the events the entire simulation. [b] Calculated from only the steady-state regime.
[c] Nonzero current or conductance that could not be meaningfully calculated, because it represents only 1 or 2 events.

events are observed during this simulation, and from ~3.3 ns onwards the charge movement data show a linear appearance. The current for this steady-state regime is calculated to be 4.9 e ns^{-1}, equivalent to 790 pA.

Other simulations, both restrained and unrestrained, generally showed a significant number of conduction events as long as the applied field was fairly large. Fig. 1.9A and table 1.1 summarize these results. Most of the conduction events—including all events in the low salt system—involved chloride ions. It should also be noted that not all the conduction events occurred in a steady-state regime, which is clear from fig. 1.9A. In several cases, particularly U–100 and U^h–100, a current was observed early in the simulation, but the steady state of these simulations involved a very low current (fig. 1.9A–C). The discrepancy between steady-state currents in +100 and –100 mV/nm fields is discussed below.

Relating the calculated currents to the transmembrane potential allows for the determination of channel conductance. As seen in previous simulations, the transmembrane potential is equivalent to the potential drop across the entire periodic box [34, 35]. This phenomenon arises because the bath solution is a highly conductive environment compared to the membrane, so there is no potential difference throughout the aqueous region. Therefore, the entirety of the potential drop across the box is concentrated across the bilayer and protein, as discussed in more detail below. Therefore, the transmembrane potential ΔV_z can be determined as follows:

$$\Delta V_z = E_z L_z \tag{1.1}$$

where E_z is the constant electric field and L_z is the length of the simulation box in the z direction (very nearly 11.0 nm for all simulations). Therefore, for fields of +100, +50, +20, 0, –50, and –100 mV/nm, ΔV_z is 1100, 550, 220, 0, –550, and –1100 mV.

Single channel conductances calculated from the currents and transmembrane potentials for each simulation are shown in table 1.1. *U+100* and *H+100* have calculated conductance values of ~0.75 nS, close to experiment (1 nS). *R+100* and *M+100* have slightly lower conductances, although they are still within a factor of 2.5. Thus, in a field of +100 mV/nm, the conductance agrees quite well with experiment. Since the protein in these simulations shows only minor structural deviation from the crystal structure (fig. 1.5C–E), it is clear that the MscS crystal structure conformation can sustain a conductance that is consistent with the experimentally observed value.

The steady-state conductance measurements from –100 mV/nm fields are much lower than those from +100 mV/nm fields, indicating a deviation from Ohm's Law. This is most obviously revealed in the conduction data (table 1.1), but is also apparent from
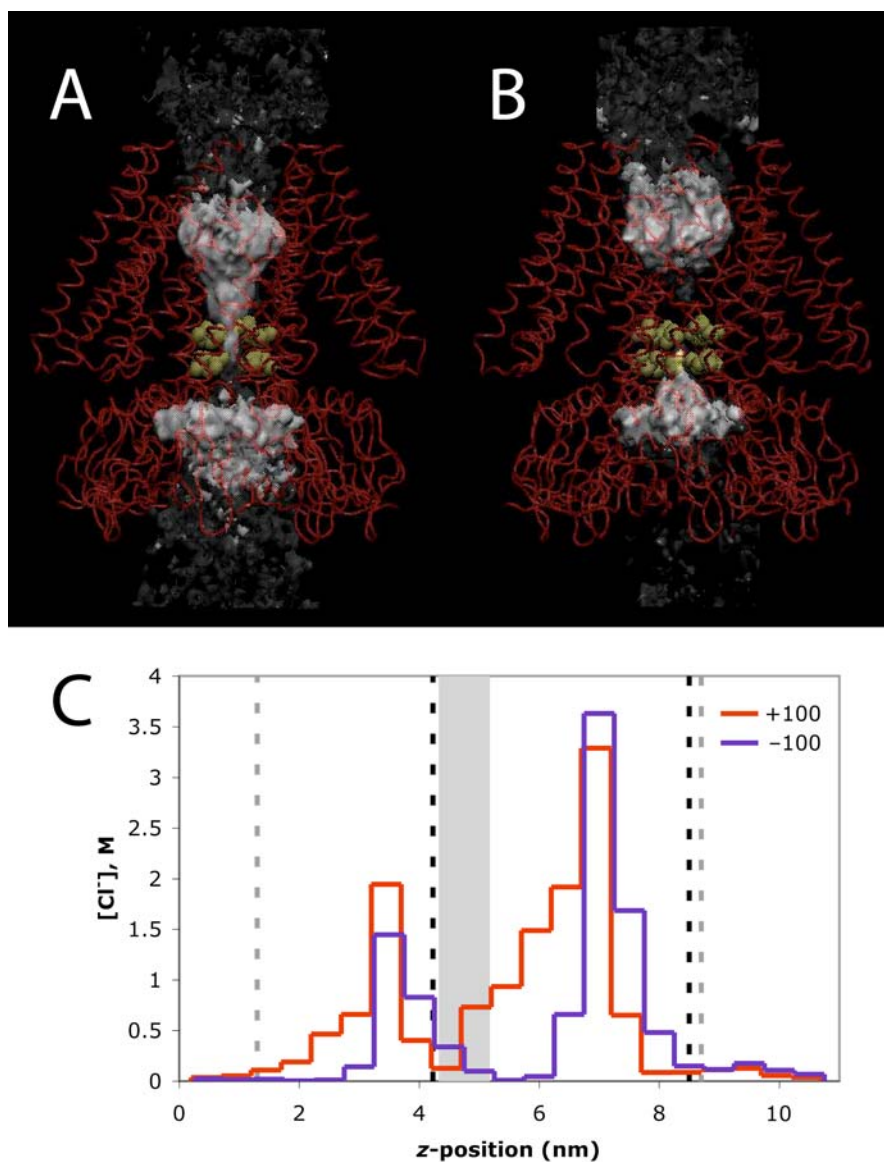
Fig 1.10. *A–B*, Time-averaged chloride density in the restrained simulations in fields of +100 (*A*) and –100 mV/nm (*B*). The regions with local concentrations of 1.33 M (opaque white) and 0.33 M (diffuse gray) are shown. The protein is shown in red, and L105 and L109 are shown in yellow spacefilling. *C*, The average chloride concentration in 0.25 nm slices of the channel region. Important regions of the simulation system are marked as in fig. 1.7D.

the local chloride concentrations (fig. 1.10). It is clear that the pore in a field of

+100 mV/nm (fig. 1.10A) has a higher average chloride concentration than in a field of

–100 mV/nm (fig. 1.10B). However, the discrepancy in the currents and conductances in

opposite fields is not because of changes in the inherent conductance of the channel.

Instead, it is due to the fact that the current in the negative but not the positive fields is limited by diffusion, as discussed in the following section.

Diffusion Properties of Chloride Ions

The discrepancy in steady-state conduction currents between +100 and –100 mV/nm fields can be attributed to the differing abilities of the protein to resupply charge carriers to the periplasmic vestibule (the chloride source for conduction in positive fields) versus the cytoplasmic vestibule (the chloride source for conduction in negative fields). In any channel, a current can be sustained only if the arrival of new charge carriers at the channel's mouth is fast enough to replenish the ions that are conducted. The rate of diffusion to the mouth, therefore, is an upper limit on the current that a channel can sustain. Applying larger potentials cannot increase the current beyond this limit, so when currents are near the diffusion rate, the channel no longer follows Ohm's Law [1].

Diffusion currents (the flow of ions into the vestibules before their conduction) can be calculated in a manner similar to conduction current. Fig. 1.9B and table 1.1 summarize the data. The differences in diffusion into the periplasmic and cytoplasmic vestibules are immediately obvious. For *R+100*, R^h+100, and *U+100*, we observe relatively large diffusion currents into the periplasmic vestibule. However, in the steady-state regimes of *R–100*, *U–100*, and $U^h–100$, there are no diffusion events into the cytoplasmic vestibule. These observations lead to the conclusion that diffusion can adequately resupply chloride ions to the periplasmic vestibule under positive potentials,

but chloride ion flow into the cytoplasmic vestibule at negative potentials is limited by the rate of diffusion.

To verify this idea, the diffusion rates in the simulations with higher salt concentrations were compared to those in the low-salt simulations. If the conduction current is determined by the inherent conductance of the channel (Ohm's Law), increasing the concentration of the charge carriers should have no effect. However, if it is dictated by diffusion, increasing the concentration of the charge carriers should lead to increased conduction currents.

The former case is observed for fields of +100 mV/nm. For both *M+100* and *H+100*, the conduction and diffusion currents are reasonably close to those in *R+100* and *U+100* (both of which use low salt). The independence of the current on the salt concentration indicates that with a +100 mV/nm field we have not reached the diffusion-limited current. In contrast, whereas the steady-state diffusion rates for *R–100*, *U–100*, and *M–100* are essentially zero, increasing the salt concentration (*H–100*) increases the diffusion and conduction currents to measurable values (–260 pA and –220 pA). The fact that increasing the concentration of the charge carriers leads to higher currents in the –100 mV/nm field indicates that diffusion is indeed the rate-limiting factor.

Furthermore, the absolute value of the diffusion current (260 pA) is in reasonable agreement with the theoretical rate of diffusion to the cytoplasmic side of the MscS pore. The rate of diffusion of ions to a channel can be approximated as the rate of diffusion ϕ into a hemisphere of radius r spanning a channel's mouth [1]. In the absence of any gradients, this rate is determined as follows:

$$\phi = 2\pi rDc \qquad\qquad (1.2)$$

where D is the diffusion coefficient and c is the concentration of charge carriers in the solution. For MscS we estimate that the appropriate radius is 0.5 nm on both the periplasmic and cytoplasmic sides of the pore. The ionic current is carried by chloride, which in high salt is at a concentration c of 300 mM (equivalent to 0.18 ions nm^{-3}) and has an aqueous diffusion coefficient D of 2.03 nm^2 ns^{-1} [1]. Therefore,

$$\phi = 2\pi(0.5 \text{ nm})(2.03 \text{ nm}^2 \text{ ns}^{-1})(0.18 \text{ ions nm}^{-3}) = 1.2 \text{ ions ns}^{-1}.$$

As such, if there were no gradients, the maximum sustainable current by a model pore of the dimensions of MscS is 1.2 e ns^{-1}, equivalent to 180 pA. The acceptable agreement between the *H–100* currents and this theoretical diffusion rate provides further evidence that diffusion limits the negative current in –100 mV/nm fields.

The local chloride concentrations also reveal the discrepancy in the rates of diffusion into the two vestibules (fig. 1.10). In fields of +100 mV/nm, there is significant chloride density throughout the region at the interface of the bulk solution and the periplasmic vestibule. In contrast, in fields of –100 mV/nm, the average chloride concentration at the interface of the bulk and the cytoplasmic vestibule is very low.

Because diffusion issues are not a concern in the +100 mV/nm simulations, it is appropriate to use these for an accurate determination of the conductance of MscS in our simulations. As mentioned earlier, the calculated value from these simulations is in good agreement with experiment. It is also worth noting that in the initial phase of U^h–100, when there are ample charge carriers in the cytoplasmic vestibule, the conductance of the channel is 0.71 nS, very near to that for *U+100* (fig. 1.9C). Only when the charge carriers are depleted (and not replenished by diffusion) does the current drop to its low steady-state value.

It should be noted that MscS in the simulation system is truncated after the middle-β domain (fig. 1.1B–C). The cytoplasmic vestibule is surrounded by the seven middle-β domains on the sides but is open on the bottom. In contrast, the cytoplasmic vestibule in full-length MscS is surrounded by the middle-β domains and the large C-terminal domains, with only small portals allowing ions to enter [23]. Thus, the full-length protein provides an even larger physical barrier to ionic diffusion into the cytoplasmic vestibule than does the model, and it is likely that the simulations overestimate the rate of diffusion of ions into the cytoplasmic vestibule. In addition, there are 26 disordered residues at the N-terminus of the crystal structure, which are not included in the simulation [23]. Because there is no known structure for this region, it is not clear how it influences diffusion rates into the periplasmic domain.

Potential Profile of the Simulation System

In the +100 mV/nm simulations, we observe diffusion currents that are significantly larger than the theoretical maximum of 180 pA. Therefore, in contrast to the cytoplasmic vestibule, the periplasmic vestibule must be an attractive sink for chloride ions. This is seen more clearly from analysis of the potential profile of the channel.

For each of the six applied electric fields, we determined the electric potential profile of the restrained simulation system (fig. 1.11). As mentioned above, like previous descriptions of transmembrane potentials, the entirety of the potential drop of the periodic box occurs in the actual transmembrane region [34, 35]. However, the protein environment causes the potential to deviate from the linear drop that would be expected for a homogeneous aqueous channel [35]. In our system, almost the entirety of the
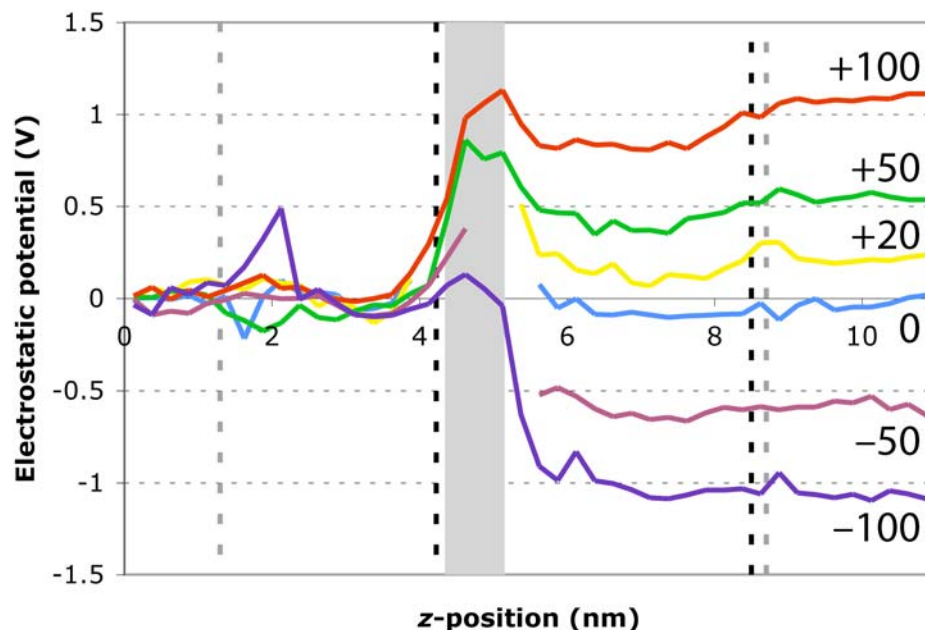
Fig. 1.11. Negative-ion electrostatic potential profiles for the simulation system under various electric fields in the R and R^h simulations. The plots for some fields are incomplete because no chloride ions were found in the pore region in some simulations. Important regions of the simulation system are marked as in fig. 1.7D.

potential drop occurs in the very narrow region of the pore. In addition, the relatively higher potential in this region indicates a significant barrier for chloride movement in either direction. This is undoubtedly due to the partial desolvation of the ion as it passes through the pore, as discussed below.

The protein provides different environments in the vestibules on either side of the pore. The periplasmic vestibule of the protein has a lower potential than the periplasmic bulk, most likely because of favorable interactions with the cationic residues in the TM domains. Furthermore, there is no barrier to entry from the bulk to the vestibule. The lower potential and lack of a barrier to entry create a sink for chloride that allows for a much higher diffusion than expected from theoretical considerations. The cytoplasmic vestibule, on the other hand, provides a potential no more favorable than the bulk, and

there even appears to be a slight barrier to entry. Therefore, diffusion into this vestibule

is much slower than that into the periplasmic vestibule.

Simulations with Different Water Models and Temperature-Coupling Groups

Because simulations are only mathematical approximations, it must be

demonstrated that our results are not artifacts of the specific parameters of the system.

As discussed above, MscS simulations employing a different force field and software

package also displayed the dehydration and occlusion of the pore in the absence of a

potential and the maintenance of a wide, hydrated pore of the protein in a bilayer under

tension [27]. The similarity of our results to these is evidence that the simulated

phenomena are not simply artifacts.

To further demonstrate this, some simulations were performed using the TIP3P

instead of SPC water model, and others were performed with the water and ions in a

single temperature-coupling bath instead of separate ones. All of these simulations

resulted in the same pore hydration (fig. 1.12A–B), ion conduction (fig. 1.12C), and ion

diffusion (fig. 1.12D) behavior observed in our initial simulations. Therefore, it is very

unlikely that the results presented here are artifacts of the simulation system.

Structural Features of the Conducting Versus the Occluded States

Our results provide the opportunity to compare the structures of a conducting

form and an occluded form of the MscS channel. The contrasts are seen clearly in

snapshots of MscS in the presence of a field of +100 mV/nm, in which the pore remains
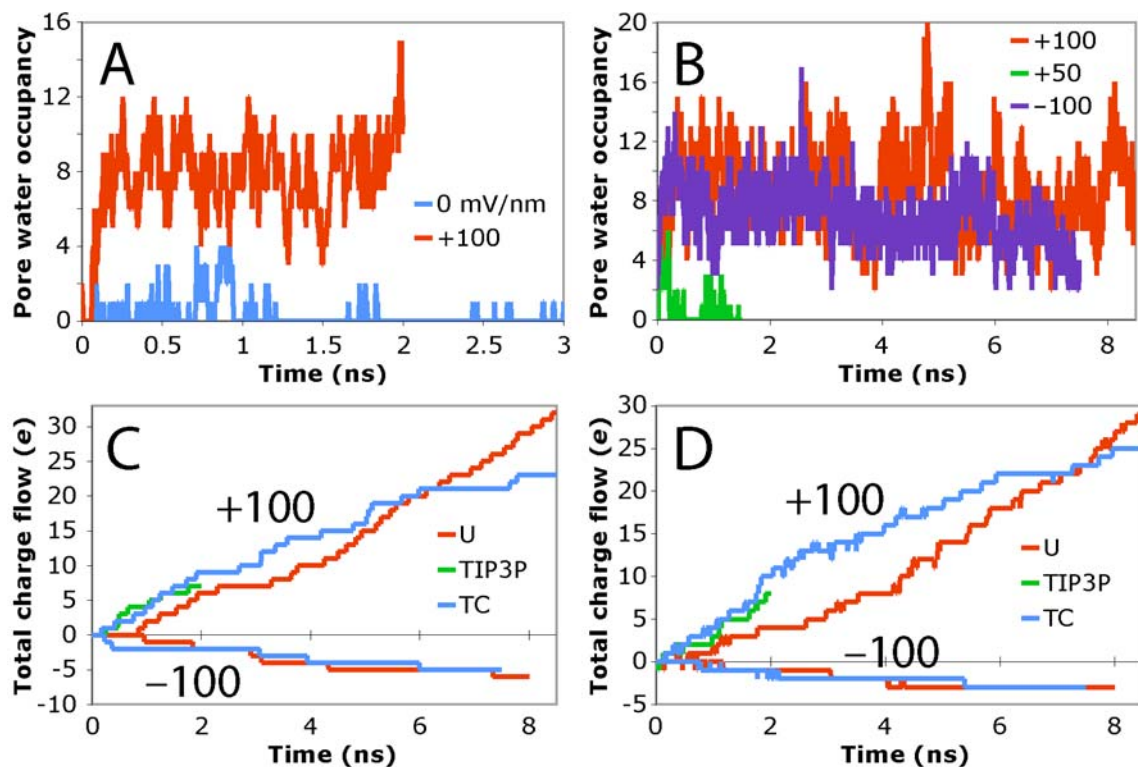
Fig. 1.12. *A*, Water occupancy of the pore in simulations using the TIP3P instead of SPC water model, with electric fields of +100 and 0 mV/nm. *B*, Water occupancy of the pore in simulations with the water and ions in a single temperature-coupling bath, with electric fields of +100, +50, and –100 mV/nm. *C–D*, Conduction (*C*) and diffusion (*D*) charge flow in simulations with fields of +100 and –100 mV/nm. U: the normal unrestrained simulations; TIP3P: simulations using TIP3P water; TC: simulations with the modified temperature-coupling baths.

fully hydrated and conducts well, and in the absence of a field, in which the pore has

collapsed (fig. 1.4D–E). We will emphasize this pair in the analysis.

In the hydrated pore, the narrowest constriction—formed by L105 and L109—

defines a pore radius of about 3 Å, similar to the crystal structure. This is the case for

both +100 and –100 mV/nm fields. When there is no water in the pore, in low or

moderate fields (–50 to +50 mV/nm), the constriction shrinks to less than 1 Å (fig. 1.13).

Later in *U+100*, the pore widens slightly beyond the original crystal structure

radius. Both the occlusion and the widening of the pore result from asymmetric motions
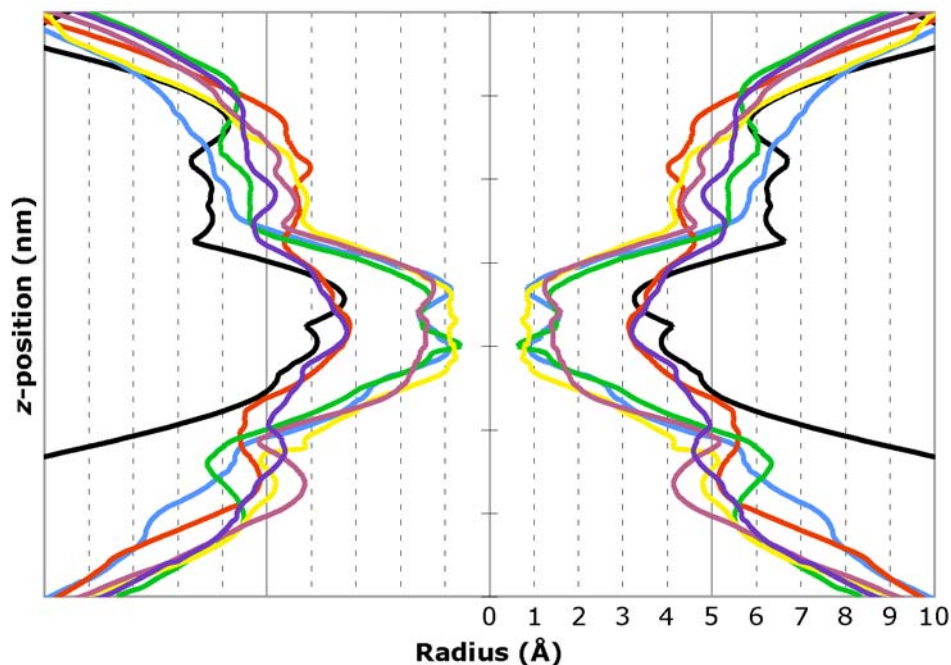
Fig. 1.13. Pore profiles, calculated by HOLE, for the crystal structure (black) and unrestrained simulations *U+100* (red), *U+50* (green), *U+20* (yellow), *U0* (blue), *U–50* (magenta), and *U–100* (purple). The profiles represent the pore at 3 ns in each simulation. Tick marks on the *y*-axis are 1 nm apart. The data have been reflected across the *y*-axis to create the appearance of a channel cross section.

of the TM3 helices. In both *U0* and *U+100*, most of the TM3 helices undergo very little lateral movement in the pore region, but significant movement of only one helix results in the different pore states (fig. 1.14A–B). In *U0*, through a reorganization of the H-bonds and the unwinding of the turn at its N-terminus, TM3 of subunit C bends and moves into the empty pore (fig. 1.14C–E). Most of the other TM3s remain about the same distance from the center. The motion of TM3-C is very similar to the motions leading to the occluded state reported by Sotomayor and Schulten [27]. In *U+100* we observe a different type of motion. During the expansion, TM3 of subunit F moves relatively far from the center, and its kink moves from G113 to A108, with a less severe kink angle (fig. 1.14F–G). A similar movement is observed for the adjacent TM3 from subunit G (fig. 1.14H). Because the timescale of the simulation is short, we cannot say that these
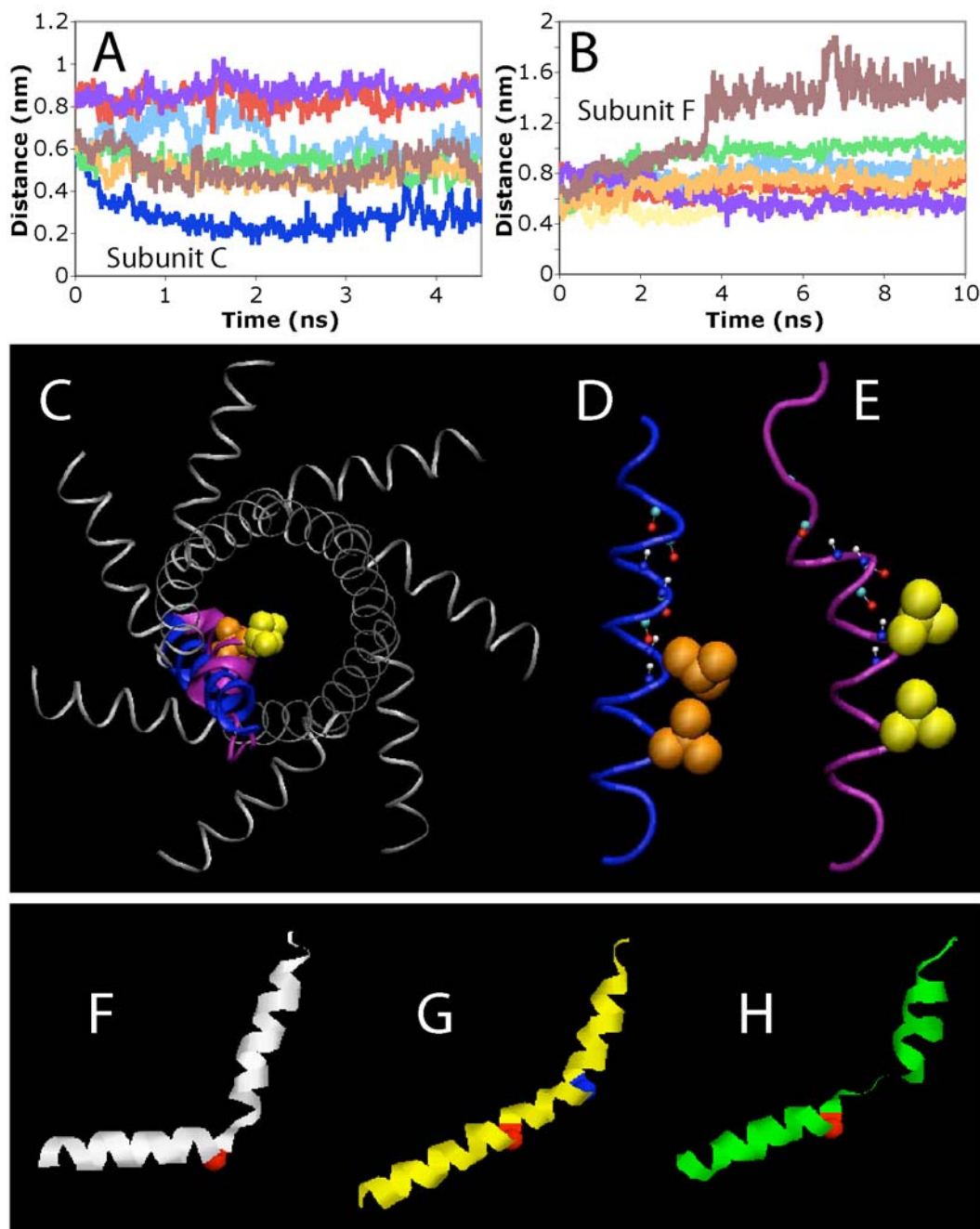
Fig. 1.14. *A–B*, Distance of each subunit from the pore center as a function of time for *U0* (*A*) and *U+100* (*B*). The distance represented is that from the center of mass of the seven L109 Cα atoms to the Cγ of L109 of each subunit. *C–E*, Snapshots of TM3 of subunit C at the beginning (blue) and end (purple) of *U0*. The sidechains of L105 and L109 are shown in spacefilling at the beginning (orange) and end (yellow) of *U0*. The view from the periplasm (*C*) shows how far the helix moves into the center of the pore. The TM3 helices of all the subunits are depicted in gray to clarify the pore at the beginning of *U0*. The side views (*D–E*) show the unwinding of the helix during the simulation. In addition, several backbone carbonyl and amide groups that begin in a normal α-helical hydrogen bonding arrangement (*D*) are broken as the helix is distorted (*E*). *F–H*, Snapshots showing side views of the TM3 helices of the E, F, and G subunits (panels *F*, *G*, and *H*, respectively) at the end of *U+100*. Red spheres represent the Cα of G113, and the blue sphere represents the Cα of A107-F, which has become the location of the helical kink. TM3-E is representative of a helix that remains similar to the crystal structure.

are relevant motions in a global conformational change, but it is notable that TM3

displays so much flexibility.

Another important structural feature is the solvation state of chloride ions as they

pass through the pore. In Anishkin and Sukharev's simulations, a chloride that is forced

to pass through the restrained MscS pore experiences a severe loss of solvation, losing all

but half of its first solvation shell [26]. The high degree of desolvation required to

conduct an ion provided some of the evidence for their claim that the MscS crystal

structure must be a nonconducting state. For our simulations, we analyzed the solvation

of the chloride ions passing through the pore by calculating their radial distribution

function (RDF) $\rho(r)$.

Fig. 1.15 shows the calculated RDF of water oxygen atoms around chloride ions

in bulk water, as well as the averaged RDF of 33 chloride ions in the steady-state phase
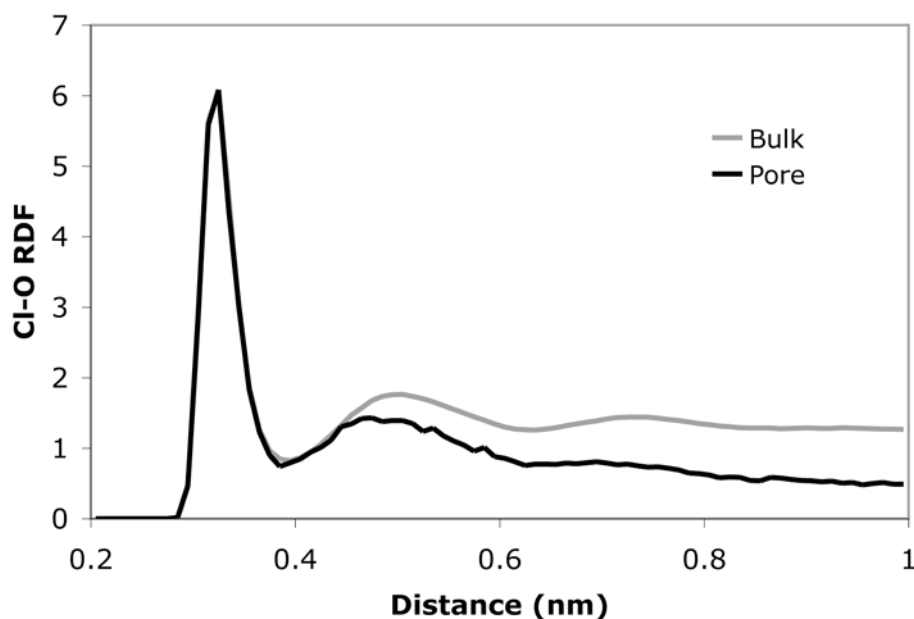
Fig. 1.15. Radial distribution functions (RDFs) of water oxygen atoms around chloride ions in the bulk and pore regions in *U+100*. The pore RDF is the average of the individual RDFs of the 33 chloride ions that were conducted in the steady-state regime, weighted by the length of time the ion spent in the pore.

of *U+100* for only the times that they were in the pore. The "pore" chloride RDF is

relatively noisy because there are fewer data points available for chloride ions in the pore

than in the bulk.

The RDF of the bulk chloride shows three distinct solvation shells, with maxima

at about 0.32, 0.50, and 0.73 nm. The number of waters present in each shell can be

determined by integration of the function $r^2\rho(r)$. For chloride in the bulk, the shells are

occupied by 7, 21, and 35 waters, respectively, although it is difficult to determine a

precise endpoint for the third shell. These results—both the radii and occupancy of the

solvation shells—agree well with those from previous experimental and computational

work [36].

The RDF for the chloride ions in the pore shows different characteristics. A

chloride in the pore does have a reduced solvation shell, but its first hydration shell is still

essentially intact. Only the second shell and beyond have a lower occupancy. Integration

of the peaks reveals that whereas the first shell has the full 7 waters, the second shell

contains only 16 waters, and there is only a faintly discernable third shell. Although this

amount of solvation is significantly less than that observed for the bulk chloride ions, it is

much greater than that reported previously [26].

Studies of Selected Mutant Channels

MscS contains a number of charged residues in its transmembrane domains,

including R46, R54, D67, R74, and R88 (fig. 1.16A). As noted above, transmembrane

arginine residues likely play an important role in voltage sensing in other ion channels, so

we performed several simulations, all completely unrestrained, of MscS mutants in which
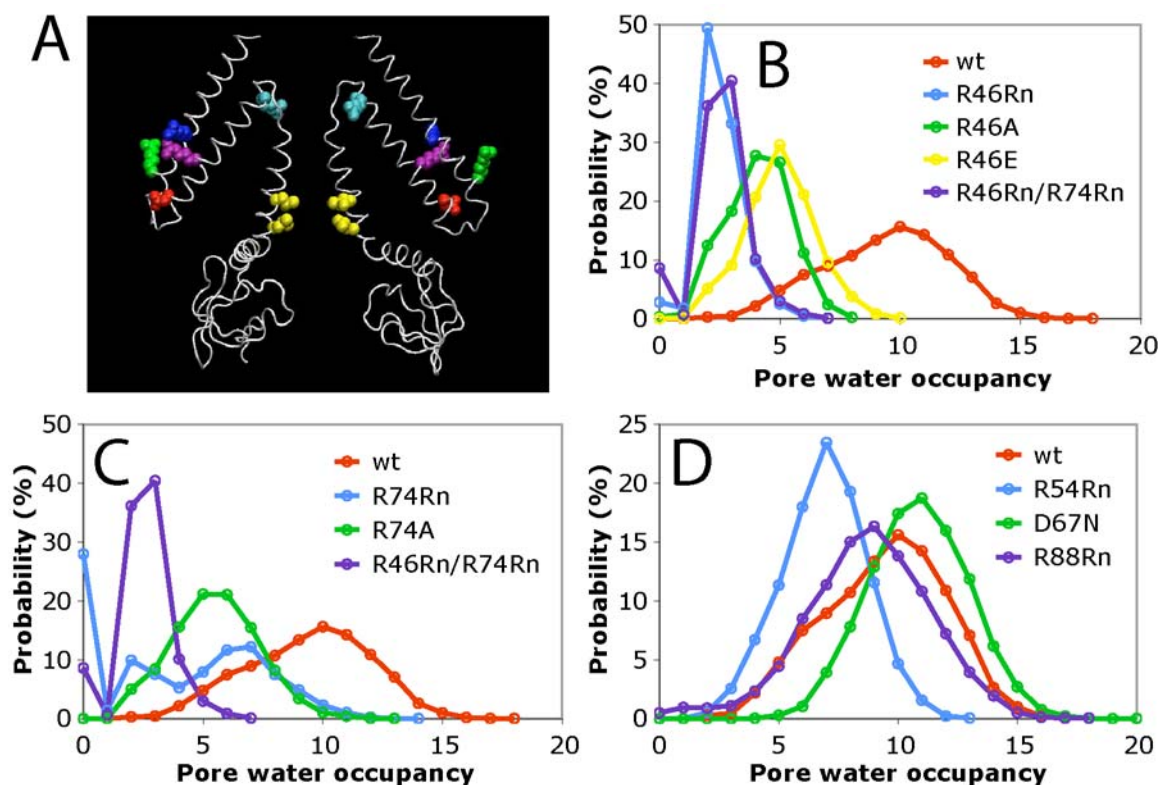
Fig. 1.16. *A*, View of the charged residues in the TM domains. Only two subunits are shown for clarity. The side chains of R46 (blue), R54 (green), D67 (red), R74 (purple), R88 (cyan), and L105 and L109 (yellow) are shown in spacefilling. *B–D*, Probability distributions of pore water occupancy in unrestrained simulations of R46 mutants (*B*), R74 mutants (*C*), and other mutants (*D*).

these charges were altered. The following mutants were studied: R46Rn, R46A, R46E, R54Rn, D67N, R74Rn, R74A, R46Rn/R74Rn, and R88Rn. Rn refers to a "neutralized arginine" residue that is missing one proton from the guanidinium group.

The water occupancies for the mutants are shown in fig. 1.16B–D. Mutations at R54, D67, and R88 do not have a substantial effect. However, mutations at R46 and R74, even to another polar residue, greatly reduce the hydration of the pore.

A possible explanation for these effects is that the charges, although distant, still contribute significantly to the electrostatic character of the pore. In model pores, partial charges greatly reduce the hydrophobicity and lead to greater pore hydration [9, 37]. In our case, the charges do not lie directly on the pore wall, but they apparently create a
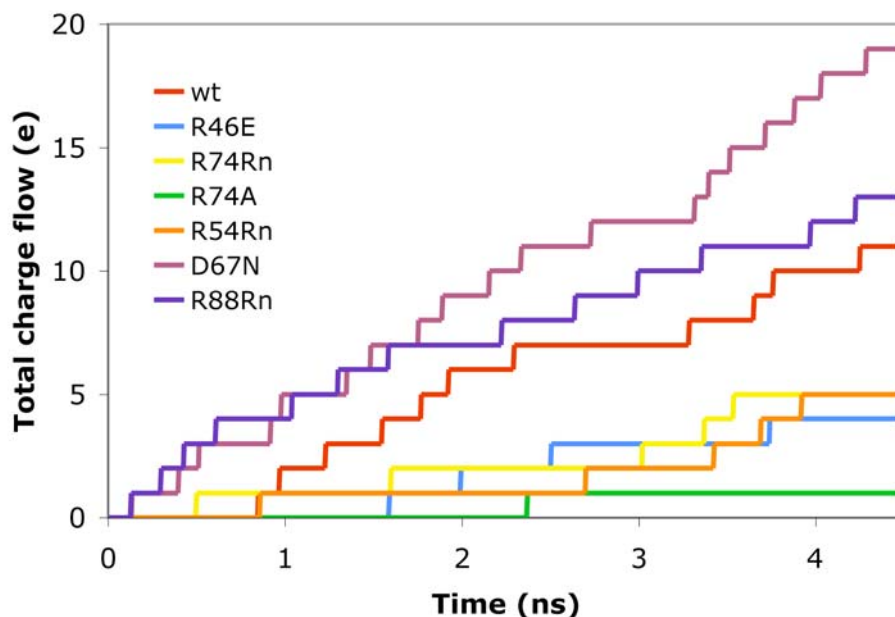
Fig. 1.17. Conductive charge movement for all the mutant simulations that produced at least one conduction event. The field in all the simulations is +100 mV/nm.

Mutant	Total Events	Steady State	
		I pA	*g* nS
wt	40	790	0.72
R46Rn	0	0	0.00
R46A	0	0	0.00
R46E	4	Low	Low
R74Rn	5	930	0.85
R74A	1	0	0.00
R46Rn/R74Rn	0	0	0.00
R54Rn	5	530	0.48
D67N	19	730	0.66
R88Rn	13	480	0.44

Table 1.2. Data on conduction currents for all mutant simulations, which contain a field of +100 mV/nm and a transmembrane potential of +1100 mV. Meanings of the headings are the same as those for table 1.1.

more hydrophilic environment. Removing the charges may make the pore more hydrophobic, thus reducing the hydration.

As expected from the fact that R54, D67, and R88 mutants have similar water behavior to wild type, conduction current data for these mutants are also reasonably close to wild type (fig. 1.17 and table 1.2). R46 and R74 mutants, on the other hand, have

lower currents, in line with the fact that they generally have less hydrated pores. R74Rn is an apparent exception to this trend, although the number of conduction events is small (only three in the steady-state regime) and probably does not accurately reflect the true conductance. These data indicate that mutations at R46 and R74 may result in loss-of-function channels.

There is no polarization built into the force field in our simulations, and there are no diffusible molecules between the transmembrane charges and the walls of the pore. Because the dielectric constant of the protein interior in our model is effectively 1, the influence of the charges is probably exaggerated. However, generally accepted values for the dielectric constant for proteins are typically quite low, in the range of 2–4 [38], so it is unlikely that the exaggeration is severe.

Investigation of the Mechanism for Voltage Modulation

Electrophysiological studies have demonstrated that voltage modulates MscS function. Early work suggested that depolarization of the membrane leads to increased open probabilities and a decreased threshold for activation by tension [14], but more recent work has indicated that voltage modulates deactivation but not activation [19]. In either case, MscS is sensitive to voltage changes. The crystal structure provided insight into a possible mechanism for this: a hinging motion of the TM1-TM2 arm that correlates lateral expansion (tension sensitivity) with upward movement of positive charges on the TM domains (voltage sensitivity) [23]. Our MD simulations shed some light on this mechanism, in that we can observe TM domain motion under the influence of different electric fields. The U simulations show that the positions of the TM1 and
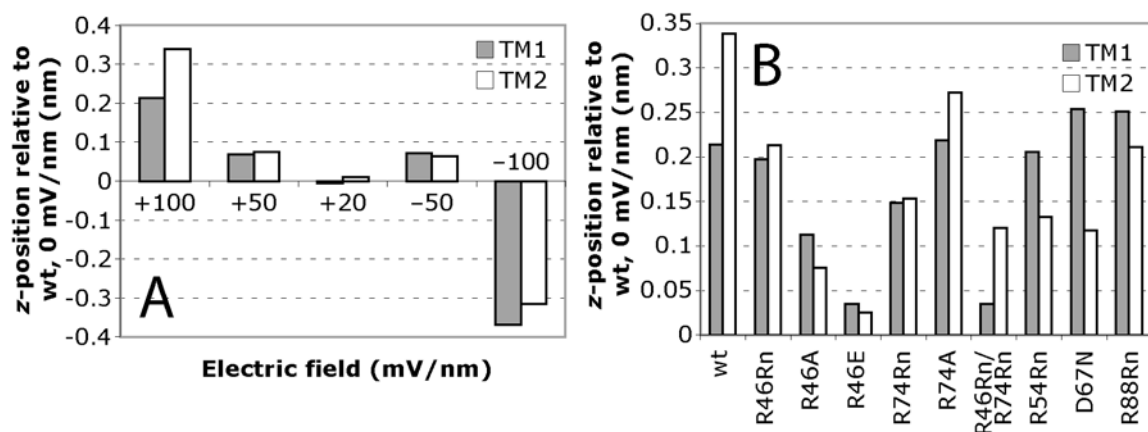
Fig. 1.18. Positions of the centers of mass for TM1 and TM2 averaged over the final 0.5 ns of some simulations, relative to that for *U0*. The positions are also corrected for fluctuations in the position of the lipid bilayer. *A*, *U* simulations of wt-MscS with different electric fields. *B*, Mutant simulations with an electric field of +100 mV/nm.

TM2 helices are indeed correlated with the field (fig. 1.18A). Relative to the unperturbed channel (in the absence of a field), the TM helices are nearer to the periplasm in the +100 mV/nm field, nearer to the cytoplasm in the –100 mV/nm field, but relatively unchanged in the low and moderate fields.

Furthermore, mutation of the charged residues within TM1 and TM2 alters the relative positions of the helices in the +100 mV/nm field in some cases (fig. 1.18B). For TM1 movement, most mutants have behavior similar to wild type (R46Rn, R74Rn, R74A, R54Rn, D67N, and R88Rn). The R46A, R46E, and R46Rn/R74Rn mutants, however, show only a slight positional change from the structure at 0 mV/nm, which suggests that R46 is the most important residue for voltage sensitivity. Mutants at this position are less responsive to transmembrane potential changes than wild type. The data for TM2 correlate reasonably well with the TM1 data, except for the R54Rn and D67N mutants, which show smaller positional changes than wild type for TM2.

It should be noted, however, that in our simulations the positions of the helices do not correlate with the hydration and conduction of the channel. In +100 and

–100 mV/nm fields, MscS contains a stably hydrated pore but has TM domains in quite different positions within the membrane. Taken together with the fact that MD simulations of only a few ns are too short to show protein conformational changes, it is not clear if the TM domain motions observed here are relevant to the activation or deactivation processes.

CONCLUSION

The MscS channel is a fascinating structure that responds to both membrane tension and transmembrane potential. The crystal structure of Rees and co-workers [23] provided many insights, but also raised intriguing questions about the relationships between structure and function in this channel. The simulations presented here confirm and expand upon previous work and also provide valuable new insights into the workings of MscS.

Both the minimalist system of Anishkin and Sukharev [26] and the much more complete model of Sotomayor and Schulten [27] concluded that, in the absence of a transmembrane potential, the crystal structure contains a "hydrophobic gate" that excludes water from the narrowest region of the channel and cannot be conducting. Our studies support that conclusion. However, this is only part of the story.

We now find that an applied voltage can prevent collapse of the unrestrained channel. Sotomayor and Schulten showed that the collapse could also be prevented if a substantial tension is applied to the membrane [27]. Importantly, in our simulations the open channel is extensively hydrated, and the degree of hydration depends on the magnitude of the voltage. This hydrated channel is able to conduct chloride ions, and the

single channel conductances seen are comparable to experimentally observed values. Much lower sodium ion conductance is seen, consistent with the known anion selectivity of the channel. Also, the severe desolvation of pore chloride ions seen by Anishkin and Sukharev is not seen here [26]. The hydrated channel under the influence of an electric field can readily accommodate a well-solvated chloride. As anticipated, preliminary simulations of mutant channels show that key transmembrane arginine residues play a critical but as yet not fully understood role in controlling the voltage sensitivity, hydration, and conductance of the channel.

To our knowledge, this is the first MD investigation of the influence of a transmembrane potential on the hydration of hydrophobic nanopores. Our results suggest that an increasing potential reduces the threshold radius for pore hydration. Although the transmembrane potentials applied in these simulations (at least 220 mV), are substantially higher than the 120–160 mV reported for bacterial membranes [32], the tensions employed by Sotomayor and Schulten are also unphysiologically high [27]. It has been noted before that, to observe effects on MD timescales, the magnitudes of external stimuli (both tension and voltage) generally must exceed the physiological range [39, 40]. Also, previous simulations of ion movement in membrane channels have used potentials as large or larger than the potentials used here [35, 41].

Of course, the simulations presented here and elsewhere are still quite approximate. The timescales are relatively short, and the force fields are imperfect. Furthermore, with a resolution of 3.9 Å and sevenfold averaging, there is still some uncertainty about precise details of the MscS structure. Nevertheless, all the observations derived from the present simulations are consistent with experimental facts, and it seems

likely that the qualitative behaviors seen here do reflect the situation under physiological conditions. Based on these observations, we conclude that the image of MscS derived from the crystal structure is more nearly that of an open, conducting state of the channel than a nonconducting state.

METHODS

Assembly of Simulation System

The initial structure for the protein, lipid, water, and ions was created as follows. The coordinates from the *E. coli* MscS crystal structure (PDB 1MXM) [23] were transformed so that the sevenfold axis was parallel to the *z*-axis. Because molecular dynamics simulations on full-length MscS would require huge amounts of CPU time due to the large number of atoms, the protein chains were truncated at the ends of the middle-β domains (fig. 1.1B), so that the model of each subunit extended from F27 (the N-terminus of the crystal structure) to S179. It is assumed that the truncated protein is a reasonable system for study because the cleaved portion, the C-terminal domain, is unlikely to strongly influence the region of interest, the pore. For all ionizable side chains, the protonation state was chosen to simulate a system at neutral pH. However, the N- and C-termini were kept neutral (NH_2 and CO_2H), reflecting the fact that the simulated peptide chains do not actually extend to the terminal residues of the protein.

The protein was embedded in a pre-equilibrated POPE bilayer model in the manner described previously [42]. SPC water was added to fill the remainder of the simulation box. Sodium and chloride ions were also added for two reasons. First, a salt solution is more physiologically relevant than a pure water solvent. Second, the large

+42 charge on the protein must be neutralized to avoid artifacts in the long-range

electrostatics algorithm [43]. Therefore, for a low-salt system that approximates a NaCl

concentration of 100 mM, 62 of the water molecules were replaced with 10 Na^+ and 52

Cl^- ions. Medium (200 mM) and high (300 mM) salt solutions contained 61 Na^+ and 103

Cl^- ions and 113 Na^+ and 155 Cl^- ion, respectively. The wild-type MscS, low-salt system

contained seven protein chains of 153 residues each, 455 POPE molecules, 28423 water

molecules, 10 Na^+ ions, and 52 Cl^- ions, for a total of 118665 atoms (fig. 1.1C). The

simulation system was minimized using the steepest-descents method.

Molecular Dynamics

All minimizations and molecular dynamics were performed with GROMACS

3.1.3 and 3.1.4 software [44, 45] with the GROMACS force field supplemented by

parameters for the lipid [46]. Van der Waals and short-range electrostatics were cut off at

1.0 nm, and the long-range electrostatics were treated with the particle mesh Ewald

(PME) method of order 4 and grid spacing of 0.1 nm [43].

The minimized structures were heated to 310 K over 20 ps with heavy harmonic

position restraints [force constant: 1000 kJ/(mol nm^2)] on all Cα atoms. Once at 310 K,

the heavy restraints were maintained for 180 ps, and then gradually lifted over 330 ps.

The frame at 350 ps (of the 530 ps total), which followed equilibration with a restraining

force constant of 500 kJ/(mol nm^2), was used as the starting structure for the restrained

simulations. The final frame (at 530 ps) was used as the starting frame for the

unrestrained simulations.

In all simulations, the temperature was maintained at 310 K by coupling to Berendsen thermostats with a time constant of 0.1 ps [47]. Separate baths were used for the protein, the lipid, the solvent, the Na^+ ions, and the Cl^- ions. Likewise, pressure was maintained with anisotropic pressure coupling in each direction to a Berendsen barostat at 1 bar with a time constant of 1.0 ps [47].

Fig. 1.2 indicates the salt system, restraints, electric field, initial pore hydration state, and start and end times of each wild-type MscS simulation. In all restrained simulations, all the atoms of the protein backbone were harmonically restrained with a force constant of 418.4 kJ/(mol nm^2) [1 kcal/(mol Å^2)]. The pore at time 0 of the restrained simulation was hydrated (R^h), and simulations with electric fields of 0 and +100 mV/nm were run for 2.5 ns. The frame at 1.47 ns of the 0 mV/nm simulation, which contains a pore empty of water, was used as the initial frame for other simulations (R), with applied electric fields of +100, +50, +20, –50, and –100 mV/nm.

Unrestrained simulations of the low-salt system beginning with an empty pore (U) were performed with electric fields of +100, +50, +20, 0, –50, and –100 mV/nm. The frame at 0.87 ns of the +100 mV/nm simulation, which contains a hydrated pore, was used as the initial frame for three more unrestrained simulations (U^h) with electric fields of +50, 0, and –100 mV/nm. Unrestrained simulations with the medium-salt (M) and high-salt (H) systems were performed with electric fields of +100, 0, and –100 mV/nm.

Control simulations were also performed with the unrestrained, low-salt system. The TIP3P instead of the SPC water model was used in one series of simulations, which were performed with applied fields of 0 and +100 mV/nm. In the other series of

simulations, which were performed with fields of +50, +100, and –100 mV/nm, the water

and ions were place in a single temperature-coupling bath instead of separate ones.

Simulations with Mutant MscS

Unrestrained simulations were also performed with mutant MscS proteins under

low-salt conditions. Five charged residues in the transmembrane domains of MscS—

R46, R54, D67, R74, and R88—were explored by mutation in eight single mutants and

one double mutant: R46Rn, R46A, R46E, R54Rn, D67N, R74Rn, R74A, R46Rn/R74Rn,

and R88Rn. Rn is a neutralized arginine model in which one of the terminal protons has

been removed, eliminating the charge on the side chain. Even though this residue is

almost certainly never found *in vivo*, its parameters are available in the GROMACS force

field. All of the mutations gave structures in which a charged residue was neutralized,

except for R46E, in which the +1 charge was mutated to a –1 charge.

The mutant models were created from the initial low salt structure, and with one

exception (D67N) no additional minimization was required. For the D67N mutant, only

the lipid molecules and side chains that were within 0.5 nm of the N67 side chains were

allowed to move. In this way, the close contacts induced by the mutations were removed

while minimizing the perturbation to the initial structure. Because of the changes in the

protein charge, ions were added to the systems to restore neutrality. Simulations for all

mutants were performed with an electric field of +100 mV/nm for 4.47 ns.

Data Analysis

RMS deviations were calculated by `g_rms`. The reference group for alignment

was all Cα atoms, and the reference structure was the structure of the protein after the

energy minimization of the entire system. For each frame in the trajectory, the reference

group was aligned with that of the reference structure, and the RMS deviation for the

whole protein was calculated. The total system energies were determined by using

`g_energy`.

The pore as defined for water and ion occupancy determinations consisted of a

cylinder with radius 1.5 nm between the centers of mass of the L105 and L109 Cα atoms.

Water and ion occupancies of the pore were monitored as a function of time with the

GROMACS analysis tool `g_occupancy`. The code is not a standard part of the

GROMACS package but was a generous gift from David Bostick (University of North

Carolina).

A conduction event is defined as the full transit of an ion through the pore. The

total charge flow through the pore was monitored by keeping a running total of the

conduction events in each simulation. A steady-state regime of the simulation was

usually easily discernable as a linear region in the plot of total charge flow as a function

of time. The slope of the function in each steady-state regime represents the average

current, which was determined by dividing the cumulative charge flow by the time

between the first and last conduction events. Currents in MD simulations have been

calculated previously using a qualitatively similar technique [34].

Diffusion currents were calculated similarly. A diffusion event was defined as the

movement of an ion into a vestibule. The periplasmic vestibule was defined as a cylinder

of radius 1.5 nm between the centers of mass of the Cα of L105 and V91, and the

cytoplasmic vestibule as a cylinder of radius 1.5 nm between the centers of mass of the

Cα of L109 and G140 (fig. 1.1B). The cumulative number of diffusion events was

plotted as a function of time, and the steady-state diffusion current was calculated by

dividing the number of diffusion events by the time between the first and last events.

The net alignment of the water as a function of position in the simulation system

was determined with `g_h2order`. Only the water molecules that occupied the pore at

some point in a given trajectory were included in the calculation. This restriction was

imposed because the *z*-position of the pore was quite close the cytoplasmic side of the

bilayer, and the net alignment of the water in the pore would have been swamped by the

many water molecules penetrating the headgroup region of the membrane.

The interaction energy distributions of the water in the pore of the restrained

simulation systems with fields of 0, +20, +50, and +100 mV/nm were determined from at

least 5000 individual interaction energies in each simulation. The individual interaction

energies were calculated as the difference between the total energy of the system in a

given frame of the trajectory with and without the water molecule. For each frame, the

total energy was calculated using `g_energy`, and the pore water molecules were

identified. One by one, they were manually removed from the system, and the energy

was recalculated. Finally, the interaction energy distributions were shifted to account for

the orientation energy of the water dipoles with the electric field. The orientation energy

of a dipole of magnitude *d* with a field of magnitude *E* is

$$Energy = -Ed\cos\theta \qquad\qquad (1.3)$$

where θ is the angle between the two vectors [48]. The average orientation energy for an ensemble of water molecules in the pore follows:

$$Energy = -E\langle N\rangle d\langle \cos\theta\rangle \qquad (1.4)$$

where $\langle N\rangle$ is the expectation value for the occupancy of the pore. $\langle N\rangle$ was calculated from the probability distribution of the water occupancies (shown in fig. 1.4C), and $\langle \cos\theta\rangle$ is the net alignment, determined above.

The local chloride density was determined using gridcount, which is not part of the standard GROMACS package but is available for download on the contributions website (http://www.gromacs.org/contributions/index.php).

Electric potential profiles for negative ions for each of the six applied electric fields were determined for the restrained simulation system by calculating the average electrostatic energy of a chloride ion as a function of its position in the box. Chloride ions that sampled different regions of the simulation system were selected for analysis, but only for the times that they remained within approximately 2 nm of the protein's sevenfold axis. For the selected chloride ions, both the z-position (determined by g_traj) and the electrostatic energy between the ion and the rest of the system were computed at each time in the simulation. The calculation of the electrostatic energy was performed in the following manner. The trajectory of a simulation was rerun with nonstandard energy groups consisting of the single chloride ion of interest and the rest of the system. The short-range electrostatic energy was obtained using g_energy. However, the long-range electrostatic energy calculated by the PME algorithm cannot be broken down into separate energy components between particular atoms; it merely contributes a system-wide long-range electrostatic energy term to the total energy. To

overcome this complication, the trajectory was rerun a second time, with the charge of the chloride of interest artificially set to 0 (with `tpbconv -zeroq`). The difference between the total long-range electrostatic energies (obtained using `g_energy`) for the two rerun trajectories was the long-range energy for the chloride ion and the system. The sum of the short-term and long-term electrostatic energies was the total electrostatic energy. The energy values were placed in bins of width 0.25 nm according to their corresponding z-positions, and the average energy was calculated for each bin. The energy purely due to the electric field, which depends only on the z-position, was added to the bin's average energy to obtain the final potential as a function of position. For some electric fields, no chloride ions were ever found in the pore region, so the potential profiles were incomplete.

Pore radii were calculated by HOLE [49], which moves a flexible balloon along the length of the channel, and at each point, calculates the largest radius that can be accommodated.

Radial distribution functions (RDFs) were calculated using `g_rdf`. For the RDFs of just the chlorides in the pore, `g_occupancy` was used to determine the exact times that each chloride occupied the pore, and the RDF for this chloride was determined for only those times. The final RDF of the pore chlorides was calculated as a weighted average of the individual RDFs, weighted by the total number of timepoints from which the RDF was calculated.

TM1 and TM2 movements of wild-type and mutant MscS were analyzed in the following manner. For each simulation, the z-positions of the centers of mass of all the atoms in TM1, TM2, and lipid as a function of time were determined. For each time, the

position of the lipid was subtracted from the positions of the TMs. The average of these differences over the last 500 ps of the simulation was calculated as the TM position relative to the lipid. Finally, these relative positions were compared to the relative position determined for *U0*.

Images were prepared with VMD [50] and Rasmol.

Computers

Three computers were used for all of the simulations: Blackrider, a dual processor Dell Precision 530 running GROMACS 3.1.3 on a Red Hat Linux 7.1 operating system (OS); Strongbad, a dual processor Dell Precision 450 running GROMACS 3.1.4 on a Red Hat Linux 8.0 OS; and Liligor, a dual processor Dell Precision 420 running GROMACS 3.1.4 on a Red Hat Enterprise Linux OS. Typical speeds of MD simulations with the MscS system were 78, 86, and 34 ps/day on Blackrider, Strongbad, and Liligor, respectively.

REFERENCES

1. Hille, B. 2001. *Ion Channels of Excitable Membranes, Third Edition.* Sunderland, MA: Sinauer Associates, Inc.

2. Zhou, Y., J. H. Morais-Cabral, A. Kaufman, and R. MacKinnon. 2001. Chemistry of ion coordination and hydration revealed by a K+ channel-Fab complex at 2.0 A resolution. *Nature*. 414:43-48.

3. Betanzos, M., C. S. Chiang, H. R. Guy, and S. Sukharev. 2002. A large iris-like expansion of a mechanosensitive channel protein induced by membrane tension. *Nat. Struct. Biol.* 9:704-710.

4. Sukharev, S. 2002. Purification of the small mechanosensitive channel of *Escherichia coli* (MscS): the subunit structure, conduction, and gating characteristics in liposomes. *Biophys. J.* 83:290-298.

5. Song, L., M. R. Hobaugh, C. Shustak, S. Cheley, H. Bayley, and J. E. Gouaux. 1996. Structure of staphylococcal alpha-hemolysin, a heptameric transmembrane pore. *Science*. 274:1859-1866.

6. Evans, R. 1990. Fluids adsorbed in narrow pores—phase-equilibria and structure. *J. Phys.: Condens. Matter*. 2:8989-9007.

7. Beckstein, O., P. C. Biggin, and M. S. P. Sansom. 2001. A hydrophobic gating mechanism for nanopores. *J. Phys. Chem. B*. 105:12902-12905.

8. Beckstein, O., and M. S. Sansom. 2003. Liquid-vapor oscillations of water in hydrophobic nanopores. *Proc. Natl. Acad. Sci. USA*. 100:7063-7068.

9. Beckstein, O., and M. S. Sansom. 2004. The influence of geometry, surface character, and flexibility on the permeation of ions and water through biological pores. *Phys. Biol*. 1:42-52.

10. Corry, B. 2006. An energy-efficient gating mechanism in the acetylcholine receptor channel suggested by molecular and brownian dynamics. *Biophys. J*. 90:799-810.

11. Wan, R., J. Li, H. Lu, and H. Fang. 2005. Controllable water channel gating of nanometer dimensions. *J. Am. Chem. Soc*. 127:7166-7170.

12. Hummer, G., J. C. Rasaiah, and J. P. Noworyta. 2001. Water conduction through the hydrophobic channel of a carbon nanotube. *Nature*. 414:188-190.

13. Levina, N., S. Totemeyer, N. R. Stokes, P. Louis, M. A. Jones, and I. R. Booth. 1999. Protection of *Escherichia coli* cells against extreme turgor by activation of MscS and MscL mechanosensitive channels: Identification of genes required for MscS activity. *EMBO J*. 18:1730-1737.

14. Martinac, B., M. Buechner, A. H. Delcour, J. Adler, and C. Kung. 1987. Pressure-sensitive ion channel in *Escherichia coli*. *Proc. Natl. Acad. Sci. USA*. 84:2297-2301.

15. Hamill, O. P., and B. Martinac. 2001. Molecular basis of mechanotransduction in living cells. *Physiol. Rev*. 81:685-740.

16. Kloda, A., and B. Martinac. 2002. Mechanosensitive channels of bacteria and archaea share a common ancestral origin. *Eur. Biophys. J*. 31:14-25.

17. Pivetti, C. D., M. R. Yen, S. Miller, W. Busch, Y. H. Tseng, I. R. Booth, and M. H. Saier, Jr. 2003. Two families of mechanosensitive channel proteins. *Microbiol. Mol. Biol. Rev*. 67:66-85.

18. Haswell, E. S., and E. M. Meyerowitz. 2006. MscS-like proteins control plastid size and shape in *Arabidopsis thaliana*. *Curr. Biol*. 16:1-11.

19. Akitake, B., A. Anishkin, and S. Sukharev. 2005. The "dashpot" mechanism of stretch-dependent gating in MscS. *J. Gen. Physiol.* 125:143-154.

20. Long, S. B., E. B. Campbell, and R. MacKinnon. 2005. Voltage sensor of Kv1.2: Structural basis of electromechanical coupling. *Science*. 309:903-908.

21. Booth, I. R., M. D. Edwards, and S. Miller. 2003. Bacterial ion channels. *Biochemistry*. 42:10045-10053.

22. Long, S. B., E. B. Campbell, and R. MacKinnon. 2005. Crystal structure of a mammalian voltage-dependent Shaker family K+ channel. *Science*. 309:897-903.

23. Bass, R. B., P. Strop, M. Barclay, and D. C. Rees. 2002. Crystal structure of *Escherichia coli* MscS, a voltage-modulated and mechanosensitive channel. *Science*. 298:1582-1587.

24. Elmore, D. E., and D. A. Dougherty. 2001. Molecular dynamics simulations of wild-type and mutant forms of the *Mycobacterium tuberculosis* MscL channel. *Biophys. J*. 81:1345-1359.

25. Elmore, D. E., and D. A. Dougherty. 2003. Investigating lipid composition effects on the mechanosensitive channel of large conductance (MscL) using molecular dynamics simulations. *Biophys. J*. 85:1512-1524.

26. Anishkin, A., and S. Sukharev. 2004. Water dynamics and dewetting transitions in the small mechanosensitive channel MscS. *Biophys. J*. 86:2883-2895.

27. Sotomayor, M., and K. Schulten. 2004. Molecular dynamics study of gating in the mechanosensitive channel of small conductance MscS. *Biophys. J*. 87:3050-3065.

28. Chanda, B., O. K. Asamoah, R. Blunck, B. Roux, and F. Bezanilla. 2005. Gating charge displacement in voltage-gated ion channels involves limited transmembrane movement. *Nature*. 436:852-856.

29. Cuello, L. G., D. M. Cortes, and E. Perozo. 2004. Molecular architecture of the KvAP voltage-dependent K+ channel in a lipid bilayer. *Science*. 306:491-495.

30. MacKinnon, R. 2004. Voltage sensor meets lipid membrane. *Science*. 306:1304-1305.

31. Posson, D. J., P. H. Ge, C. Miller, F. Bezanilla, and P. R. Selvin. 2005. Small vertical movement of a K+ channel voltage sensor measured with luminescence energy transfer. *Nature*. 436:848-851.

32. Kashket, E. R. 1985. The proton motive force in bacteria—a critical-assessment of methods. *Annu. Rev. Microbiol*. 39:219-242.

33. Bostick, D., and M. L. Berkowitz. 2003. The implementation of slab geometry for membrane-channel molecular dynamics simulations. *Biophys. J.* 85:97-107.

34. Aksimentiev, A., and K. Schulten. 2005. Imaging alpha-hemolysin with molecular dynamics: ionic conductance, osmotic permeability, and the electrostatic potential map. *Biophys. J.* 88:3745-3761.

35. Crozier, P. S., D. Henderson, R. L. Rowley, and D. D. Busath. 2001. Model channel ion currents in NaCl-extended simple point charge water solution with applied-field molecular dynamics. *Biophys. J.* 81:3077-3089.

36. Chandrasekhar, J., D. C. Spellmeyer, and W. L. Jorgensen. 1984. Energy component analysis for dilute aqueous-solutions of Li+, Na+, F-, and Cl- ions. *J. Am. Chem. Soc.* 106:903-910.

37. Lu, J., and M. E. Green. 1997. Simulation of water in a pore with charges: Application to a gating mechanism for ion channels. *Progr. Colloid Polym. Sci.* 103:121-129.

38. Harvey, S. C. 1989. Treatment of electrostatic effects in macromolecular modeling. *Proteins*. 5:78-92.

39. Gullingsrud, J., D. Kosztin, and K. Schulten. 2001. Structural determinants of MscL gating studied by molecular dynamics simulations. *Biophys. J.* 80:2074-2081.

40. Tieleman, D. P., H. J. Berendsen, and M. S. Sansom. 2001. Voltage-dependent insertion of alamethicin at phospholipid/water and octane/water interfaces. *Biophys. J.* 80:331-346.

41. Ramakrishnan, V., D. Henderson, and D. D. Busath. 2004. Applied field nonequilibrium molecular dynamics simulations of ion exit from a beta-barrel model of the L-type calcium channel. *Biochim. Biophys. Acta*. 1664:1-8.

42. Faraldo-Gomez, J. D., G. R. Smith, and M. S. Sansom. 2002. Setting up and optimization of membrane protein simulations. *Eur. Biophys. J.* 31:217-227.

43. Essmann, U., L. Perera, M. L. Berkowitz, T. Darden, H. Lee, and L. G. Pedersen. 1995. A smooth particle mesh Ewald method. *J. Chem. Phys.* 103:8577-8593.

44. Berendsen, H. J. C., D. Vanderspoel, and R. Vandrunen. 1995. Gromacs—A message-passing parallel molecular-dynamics implementation. *Comput. Phys. Comm.* 91:43-56.

45. Lindahl, E., B. Hess, and D. van der Spoel. 2001. GROMACS 3.0: A package for molecular simulation and trajectory analysis. *J. Mol. Mod.* 7:306-317.

46. Berger, O., O. Edholm, and F. Jahnig. 1997. Molecular dynamics simulations of a fluid bilayer of dipalmitoylphosphatidylcholine at full hydration, constant pressure, and constant temperature. *Biophys. J.* 72:2002-2013.

47. Berendsen, H. J. C., J. P. M. Postma, W. F. Vangunsteren, A. Dinola, and J. R. Haak. 1984. Molecular-dynamics with coupling to an external bath. *J. Chem. Phys.* 81:3684-3690.

48. Israelachvili, J. 1991. *Intermolecular & Surface Forces, Second Edition.* London: Academic Press.

49. Smart, O. S., J. Breed, G. R. Smith, and M. S. Sansom. 1997. A novel method for structure-based prediction of ion channel conductance properties. *Biophys. J.* 72:1109-1126.

50. Humphrey, W., A. Dalke, and K. Schulten. 1996. VMD: Visual molecular dynamics. *J. Mol. Graph.* 14:33-38.